

Real-space approach for the Euler class and fragile topology in quasicrystals and amorphous lattices

Dexin Li¹, Citian Wang¹ and Huaqing Huang^{1,2,3*}

¹ School of Physics, Peking University, Beijing 100871, China

² Collaborative Innovation Center of Quantum Matter, Beijing 100871, China

³ Center for High Energy Physics, Peking University, Beijing 100871, China

* huaqing.huang@pku.edu.cn

Abstract

We propose a real-space formalism of the topological Euler class, which characterizes the fragile topology of two-dimensional systems with real wave functions. This real-space description is characterized by local Euler markers whose macroscopic average coincides with the Euler number, and it applies equally well to periodic and open boundary conditions for both crystals and noncrystalline systems. We validate this by diagnosing topological phase transitions in clean and disordered crystalline systems with the reality endowed by the space-time inversion symmetry \mathcal{I}_{ST} . Furthermore, we demonstrated the topological Euler phases in quasicrystals and even in amorphous lattices lacking any spatial symmetries. Our work not only provides a local characterization of the fragile topology but also significantly extends its territory beyond \mathcal{I}_{ST} -symmetric crystalline materials.

Copyright attribution to authors.

This work is a submission to SciPost Physics.

License information to appear upon publication.

Publication information to appear upon publication.

Received Date

Accepted Date

Published Date

1

2 Contents

3	1 Introduction	2
4	2 Characteristic class in k- versus r-space	3
5	3 Remarks on r-space Euler number	4
6	4 Tight-binding model	5
7	5 Diagnosis of Topological phase transitions	7
8	6 Fragile topology in quasicrystals and amorphous lattices	8
9	7 Conclusion	9
10	A Orientability of our models	9
11	B Derivation of Eq. (4) in the main text	10

12	C Derivation of Eq. (6) in the main text	13
13	D Numerical implementation of the real-space Euler number	15
14	E The distinction between the real-space Chern and Euler numbers	16
15	F Averaging the local Euler marker in finite systems with OBC	17
16	G Brief discussion of the reality condition in \mathcal{PT}-broken systems	20
17	H Details of the model and method	20
18	H.1 Model	20
19	H.2 Disorder of on-site energy	21
20	H.3 Structural disorder	22
21	H.4 Twisted boundary condition for quasicrystals	22
22	H.5 Construction of composite Wannier function	22
23	H.6 Numerical calculation of the k-space Euler number	23
24	I More numerical results	24
25	I.1 Band structures around the topological phase transition in Fig. 1(b)	24
26	I.2 Convergence of the real-space Euler number with decreasing band gap	24
27	I.3 Convergence of the real-space Euler number with increasing lattice size	24
28	I.4 Deviation of real-space Euler number with OBC	25
29	I.5 Local Euler markers in lattices with on-site disorder in Fig. 1(c)	25
30	I.6 Euler insulator in lattice with moderate structural disorder	28
31	I.7 The upward shift of eigenenergies of corner states with decreasing bulk gap	29
32	I.8 Validation in other models with different Euler numbers	29
33	References	32

34
35

36 1 Introduction

37 Topological phases have garnered attention for their unique properties, originating with the
38 integer quantum Hall effect which is characterized by the topological invariant called the
39 Chern number [1–3] and associated chiral edge modes [4, 5]. Mathematically, the Chern
40 number is derived from the Chern class, a cohomology class characterizing *complex* vector
41 bundles. Typically, Chern numbers can be determined from complex Bloch wave functions via
42 a momentum-space expression that relies on the translation invariance of crystalline solids
43 [6–9]. However, in open-boundary systems, or in the presence of disorder, the lack of transi-
44 tional invariance renders the momentum-space expression no longer available. This has led
45 to the development of a real-space representation of the Chern number [10], including local
46 Chern markers [11, 12] and the nonlocal Bott index [13, 14], which triggers extensive study
47 on the real-space characterizations of more topological states of matter [15–41].

48 Recently, novel topological phases characterized by Euler and Stiefel-Whitney classes have
49 been proposed in orientable *real* vector bundles associated with real Bloch states [42–47].
50 Physically, two-dimensional real wave functions can be topologically classified by the Stiefel-
51 Whitney numbers [48–50] which are \mathbb{Z}_2 invariants taking either 0 or 1, and each two-band
52 subspace may exhibit a fragile topology that is characterized by an integer Euler number

53 $e \in \mathbb{Z}$ [51–53]. Similar to the Chern number, the Euler number can be expressed as an integral
 54 in momentum space for real orientable two-band subsystems, and its parity is identical to the
 55 second Stiefel-Whitney number w_2 , implying a close relationship between these two classes.
 56 Unlike the Chern insulator, the fragile topology of the Euler class can be tuned by adding trivial
 57 bands, implying its non-additive feature [49, 50]. Nevertheless, such a fragile topology pro-
 58 tects the nonzero superfluid weight in twisted bilayer graphene [54]. Moreover, the Euler class
 59 also serves as non-Abelian topological invariants to characterize the band nodal braiding in
 60 multi-gap systems [55], which is in stark contrast to the single-gap Abelian topology within the
 61 ten-fold way classification [56]. Such multi-gap non-Abelian topology has been implemented
 62 in various systems such as crystalline materials [47, 57], acoustic metamaterials [58–60], and
 63 photonic systems [61–64], stimulating rapid recent progress in this ever-growing field [65–68].

64 Typically, the real Bloch states in crystals are enforced by the space-time inversion sym-
 65 metry \mathcal{I}_{ST} (time-reversal \mathcal{T} combined with inversion \mathcal{P} or two-fold rotation \mathcal{C}_{2z}) [69], which
 66 can be destroyed locally in the presence of disorder. Moreover, in a finite nonmagnetic sys-
 67 tem with open boundaries, \mathcal{I}_{ST} symmetry is not even essential for the reality condition. The
 68 limitation of the momentum-space formula makes it urgent to search for a local characteriza-
 69 tion of real topological phases in systems with disorder and more generally in open-boundary
 70 systems inherently lacking translation and \mathcal{I}_{ST} symmetries, such as quasicrystals [70–75] and
 71 amorphous systems [76–81].

72 In this Letter, we develop a real-space formalism for Euler class topology in 2D systems.
 73 In an analogy to the Chern class, we introduce a local Euler marker $e(\mathbf{r})$ to directly map the
 74 Euler topology in real space for both crystals and noncrystalline systems. The macroscopic
 75 average of $e(\mathbf{r})$ coincides with the Euler number regardless of periodic or open boundary con-
 76 ditions. We validate our real-space formalism by verifying topological Euler and trivial phases
 77 in clean systems, yielding consistent results with \mathbf{k} -space approaches. Additionally, we ap-
 78 ply our method to a particular \mathcal{PT} -symmetric disordered system, successfully diagnosing the
 79 disorder-induced topological phase transition. Furthermore, our real-space formalism proves
 80 powerful in characterizing fragile topological phases in quasicrystals and even in amorphous
 81 systems lacking any spatial symmetries.

82 2 Characteristic class in \mathbf{k} - versus \mathbf{r} -space

83 The Euler class is a characteristic class of oriented real vector bundles. It can be constructed us-
 84 ing an orthonormal basis $\{|u_n(\mathbf{k})\rangle\}$, where $|u_n(\mathbf{k})\rangle$ represents the cell-periodic part of the n -th
 85 occupied Bloch state $\langle \mathbf{r} | \psi_n(\mathbf{k}) \rangle = e^{i\mathbf{k} \cdot \mathbf{r}} \langle \mathbf{r} | u_n(\mathbf{k}) \rangle$. Utilizing this basis, we obtain the curvature
 86 matrix \mathcal{F} with its entries given by:

$$\mathcal{F}_{mn}(\mathbf{k}) = \langle \partial_{[k_x} u_m(\mathbf{k}) | \partial_{k_y]} u_n(\mathbf{k}) \rangle dk_x \wedge dk_y, \quad (1)$$

87 where $[\dots, \dots]$ denotes the commutator applied to the index k_x and k_y . When there are two
 88 occupied bands, the Euler class can be expressed as a differential 2-form in \mathbf{k} space,

$$\begin{aligned} e(\mathcal{F}) &= \frac{1}{2\pi} \text{Pf}(\mathcal{F}), \\ &= \frac{1}{2\pi} \langle \partial_{[k_x} u_1(\mathbf{k}) | \partial_{k_y]} u_2(\mathbf{k}) \rangle dk_x \wedge dk_y, \end{aligned} \quad (2)$$

89 where Pf denotes the Pfaffian acting on the matrix \mathcal{F} . The Euler number e is an integer topo-
 90 logical invariant for two real bands, which can be expressed as a simple \mathbf{k} -space integral [82],

$$e = \frac{1}{2\pi} \int_{BZ} \langle \partial_{[k_x} u_1(\mathbf{k}) | \partial_{k_y]} u_2(\mathbf{k}) \rangle dk_x dk_y. \quad (3)$$

91 To derive the expression of the Euler number in \mathbf{r} -space, we start by replacing the occupied
 92 states in the above expression with a projection operator $\hat{P}(\mathbf{k}) = \sum_{\text{occ}} |u_n(\mathbf{k})\rangle\langle u_n(\mathbf{k})|$ in the
 93 occupied subspace [11]. After some algebra (see appendix B), we obtain the \mathbf{k} -space formula
 94 of Euler number e represented by $\hat{P}(\mathbf{k})$,

$$e = \frac{1}{2\pi} \int_{BZ} d^2\mathbf{k} \text{Pf}_{\text{occ}}(\hat{P}(\mathbf{k})[\partial_{k_x}\hat{P}(\mathbf{k}), \partial_{k_y}\hat{P}(\mathbf{k})]), \quad (4)$$

95 where Pf_{occ} denotes the Pfaffian taken over the occupied subspace.

96 To generalize a formula of topological system defined in \mathbf{k} space to its real-space form
 97 applicable to disordered system, a standard mathematical framework is the non-commutative
 98 geometry [83], which provides the duality (see the equivalence at least for translational in-
 99 variant systems in appendix C),

$$\begin{aligned} \int_{BZ} \frac{d^2\mathbf{k}}{(2\pi)^2/A} &\rightarrow \text{Tr}, \\ \partial_{k_x}\hat{P}(\mathbf{k}) &\rightarrow \frac{L_x}{2\pi}(\hat{U}\hat{P}\hat{U}^\dagger - \hat{P}), \\ \partial_{k_y}\hat{P}(\mathbf{k}) &\rightarrow \frac{L_y}{2\pi}(\hat{V}\hat{P}\hat{V}^\dagger - \hat{P}), \end{aligned} \quad (5)$$

100 where $A = L_x L_y$ is the area of the system, $\hat{U} = \exp(2\pi i \hat{X}/L_x)$ and $\hat{V} = \exp(2\pi i \hat{Y}/L_y)$ are the
 101 unitary position operator, Tr is the trace over the coordinate space, and \hat{P} is the \mathbf{r} -space projec-
 102 tion operator. Note that the order of \hat{P} is determined by both the site coordinates $\mathbf{r}_i = (x_i, y_i)$,
 103 dependent on the lattice size, and the internal index n , matching the order of $\hat{P}(\mathbf{k})$. Therefore,
 104 we can divide the space on which \hat{P} operates into two subspaces, $S(\hat{P}) = l^2(\mathbb{T}^2) \otimes \mathbb{R}^N$. Here,
 105 $l^2(\mathbb{T}^2)$ is the coordinate space, where \mathbb{T}^2 denotes the two-torus, a rectangle with edge length
 106 L_x and L_y with periodic boundary conditions (PBC) [14]. And \mathbb{R}^N is internal space with the
 107 internal degrees of freedom N which are those degrees of freedom except for the coordinate
 108 \mathbf{k} or $\{\mathbf{r}_i\}$. Consequently, we arrive at the \mathbf{r} -space expression for the Euler number:

$$e = \frac{1}{2\pi} \text{Tr} \text{Pf}_{\text{occ}}(\hat{P}[\hat{U}\hat{P}\hat{U}^\dagger, \hat{V}\hat{P}\hat{V}^\dagger]), \quad (6)$$

109 where Pf_{occ} denotes the Pfaffian taken over the occupied submatrix in the internal space (see
 110 appendix D for more details). Formally, Eq. (6) share a similar expression to the real-space
 111 Chern number except for the substituting from Tr to Pf_{occ} . Thus analogous to prior work on
 112 the local Chern marker [11], we propose defining the local Euler marker $e(\mathbf{r})$ as the expression
 113 in Eq. (6) before taking the trace, i.e.,

$$e(\mathbf{r}) = \frac{1}{2\pi} \text{Pf}_{\text{occ}}(\langle \mathbf{r} | \hat{P}[\hat{U}\hat{P}\hat{U}^\dagger, \hat{V}\hat{P}\hat{V}^\dagger] | \mathbf{r} \rangle). \quad (7)$$

114 where $|\mathbf{r}\rangle$ denotes the basis to construct the external space indexed by the Wannier cell \mathbf{r} .
 115 The \mathbf{r} -space Euler number (6) and local Euler marker (7) apply well to both crystalline and
 116 noncrystalline systems. They not only provide an intuitive local perspective of global topology
 117 but also serve as a valuable tool for distinguishing topological phases in aperiodic systems
 118 without translational symmetry.

119 3 Remarks on \mathbf{r} -space Euler number

120 Before proceeding, we have a few remarks. First, the analysis we've conducted thus far can
 121 be directly applied to the Chern class, and the resultant \mathbf{r} -space expression is nothing but

122 the Bott index, $\text{Bott}(\hat{U}, \hat{V}) = (1/2\pi)\text{ImTr} \log(\hat{U}\hat{V}\hat{U}^{-1}\hat{V}^{-1})$ with $\hat{U} = \hat{P} \exp(2\pi i \hat{X}/L_x) \hat{P}$ and
 123 $\hat{V} = \hat{P} \exp(2\pi i \hat{Y}/L_y) \hat{P}$, which offers an equivalent topological classification to the Chern num-
 124 ber [14, 15]. However, there are significant differences between the \mathbf{r} -space formulation of the
 125 Euler and Chern number. The \mathbf{r} -space Chern number only requires a simple trace performed
 126 consistently in both coordinate and internal space. In contrast, for the \mathbf{r} -space Euler number,
 127 it becomes essential to distinguish between the coordinate and internal space, which requires
 128 trace and Pfaffian operations, respectively.

129 Secondly, to decompose the coordinate and internal spaces for extracting the occupied sub-
 130 matrix needed for Pfaffian calculation, we apply a unitary transformation to the eigenstates
 131 which makes \hat{P} block-diagonal. This unitary transformation corresponds to constructing a set
 132 of composite Wannier functions, which can be determined by an explicit algorithm of localiza-
 133 tion functional minimization proposed by Marzari and Vanderbilt [84, 85] (see appendix H.5).
 134 Importantly, while a nontrivial topological invariant may pose a topological obstruction for
 135 constructing Wannier representations composed of exponentially localized states in line with
 136 lattice symmetries [49, 51, 86, 87], it does not hinder the search for composite Wannier func-
 137 tions with optimal power-law decay [88–93].

138 Thirdly, the distinct treatments of Chern and Euler numbers in real space also lead to
 139 different behaviors in finite samples under open boundary conditions (OBC). It's well-known
 140 that the summation of the local Chern marker over an entire open system must equal zero,
 141 regardless of whether the system is a Chern insulator or not. This is because the local Chern
 142 marker in the bulk is always offset by the significant deviation at the boundary [11, 14]. In
 143 contrast, the local Euler marker near the open boundary fades away and thus doesn't suffer
 144 from the counteraction under OBC, making the choice of boundary condition irrelevant for
 145 the \mathbf{r} -space Euler number (see appendix E).

146 4 Tight-binding model

147 To numerically validate the \mathbf{r} -space formula of Euler number, we consider a general \mathcal{PT} -
 148 symmetric tight-binding model with the basis $(ip_x, ip_y, d_{xy}, d_{x^2-y^2})$ per site. The Hamiltonian
 149 is given by

$$H = \sum_{i\mu} \epsilon_\mu c_{i\mu}^\dagger c_{i\mu} + \sum_{\langle ij \rangle} \sum_{\mu\nu} t_{\mu\nu}(\mathbf{r}_{ij}) c_{i\mu}^\dagger c_{j\nu}, \quad (8)$$

150 where $c_{i\mu}^\dagger$ ($c_{i\mu}$) is electron creation (annihilation) operator on the μ orbital at the i -th site. ϵ_μ is
 151 the on-site energy and $t_{\mu\nu}(\mathbf{r}_{ij})$ is the Slater-Koster parameterized hopping integral [94, 95] and
 152 has an inverse-square decay with the distance (i.e., $|\mathbf{r}_{ij}|^{-2}$) [96] (See details in appendix H.1).
 153 It has been proven that a \mathcal{PT} -symmetric Hamiltonian can become real-valued through the
 154 Takagi decomposition [49, 97]. Here we intentionally chose the p orbitals to be imaginary,
 155 which results in $\mathcal{PT} = \hat{K}$ with the complex conjugation operator \hat{K} . The invariance of the
 156 Hamiltonian under \mathcal{PT} imposes the reality condition on H . It was previously known that a
 157 fragile topological state with a nontrivial Euler number $e = 1$ can be achieved by considering a
 158 double band inversion between $p_{x,y}$ and $d_{x^2-y^2, xy}$ orbitals [98]. Here we verify the validity of
 159 the \mathbf{r} -space Euler number in both crystalline and noncrystalline systems based on this model.
 160 We also validate our expression using other models with different Euler numbers, which are
 161 detailed in the appendix I.8.

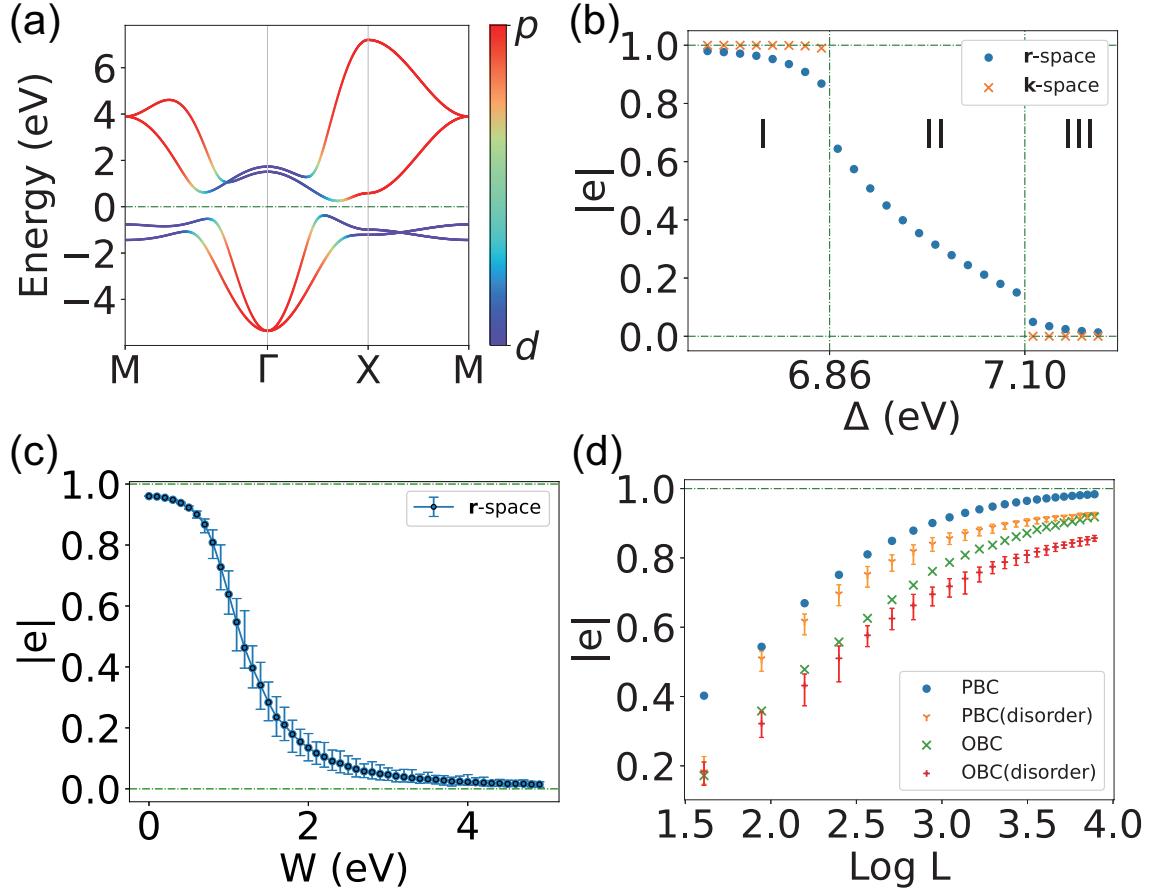


Figure 1: (a) Orbital-resolved band structures of the square lattice with a double band inversion between $p_{x,y}$ and $d_{x^2-y^2,xy}$ orbitals. The parameters used are $\epsilon_{p_x,p_y} = 1.58$, $\epsilon_{d_{x^2-y^2,xy}} = -0.42$, $V_{pp\sigma} = -0.865$, $V_{pp\pi} = -0.144$, $V_{pd\sigma} = 0.173$, $V_{pd\pi} = 0.135$, $V_{dd\sigma} = 0.144$, $V_{dd\pi} = 0.124$, $V_{dd\delta} = 0.259$ eV. (b) The variation of the Euler number as the on-site energy difference $\Delta = \epsilon_p - \epsilon_d$ changes. Other parameters remain unchanged and the lattice size is $L = 201$. (c) The r -space Euler number as a function of the disorder strength W in 31×31 square lattices with periodic boundary condition (PBC). (d) The lattice size L dependence of the r -space Euler number calculated without and with on-site energy disorder ($W = 1.0$ eV) using PBC and open boundary condition (OBC). For each L and W , the configuration average is performed over 100 realizations.

162 5 Diagnosis of Topological phase transitions

163 With the well-defined \mathbf{r} -space Euler number, we first diagnose topological phase transitions in
 164 a square lattice based on the model in Eq. (8). As shown in Fig. 1(a), the orbital-resolved band
 165 structure displays signs of a double band inversion between $p_{x,y}$ and $d_{x^2-y^2,xy}$ orbitals around
 166 the Γ point, implying their nontrivial electronic topology. We compute the Euler number in
 167 both \mathbf{k} -space and \mathbf{r} -space, consistently yielding a value of $e = 1$, thus confirming the nontrivial
 168 Euler topology. We further examine the evolution of the Euler number in both \mathbf{k} - and \mathbf{r} -
 169 spaces with increasing the on-site energy difference $\Delta = \epsilon_p - \epsilon_d$. In Fig. 1(b), the system
 170 undergoes a topological phase transition from a topological Euler insulator with $e = 1$ (region
 171 I) to an intermediate gapless state (II) and eventually transitions into a trivial insulator with
 172 $e = 0$ (III). The calculated \mathbf{r} -space Euler number matches with the \mathbf{k} -space one, except for the
 173 intermediate gapless phase (region II) where the Euler number is ill-defined. This transition
 174 can be understood by tracing the evolution of band inversion (see appendix I.1): Starting
 175 from a double inverted band order, the nontrivial energy gap gradually decreases to zero with
 176 increasing Δ , then remains closed over a finite Δ range, and eventually reopens with a trivial
 177 normal band order.

178 Next, we demonstrate the applicability of the \mathbf{r} -space Euler number for aperiodic sys-
 179 tems by introducing the disorder term in the on-site energies of the aforementioned model.
 180 We specifically consider disorder term that preserves \mathcal{PT} symmetry, which is represented by
 181 $V_{\text{dis}} = \sum_{i \in \tau_{1/2}} \lambda_i (c_i^\dagger c_i + c_{\mathcal{P}i}^\dagger c_{\mathcal{P}i})$ with the random variables $\{\lambda_i\}$ distributed uniformly within the
 182 interval $[-W, W]$ on half of the sites ($\tau_{1/2}$) in the sample, where W is the disorder strength.
 183 The annihilation operators c_i and $c_{\mathcal{P}i}$ act on the site at \mathbf{r}_i and its inversion partner $\mathcal{P}\mathbf{r}_i$, respec-
 184 tively. The averaged \mathbf{r} -space Euler number as a function of W is shown in Fig. 1(c). For mod-
 185 erate disorder, the \mathbf{r} -space Euler number e remains around 1, indicating the system remains
 186 topologically nontrivial. Remarkably, as disorder strength W increases, e gradually decreases
 187 to 0, diagnosing a topological phase transition (see appendix I.5). Our results confirm the
 188 disorder-induced topological phase transition classified by the topological Euler class [99, 100],
 189 and validate the \mathbf{r} -space formalism of Euler number in disordered systems.

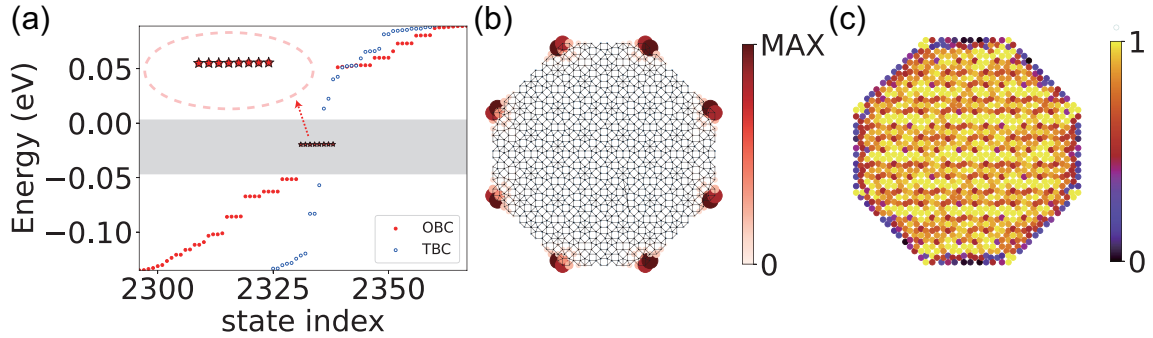


Figure 2: Fragile topological state characterized by $e = 1$ in the Ammann-Beenker-tiling quasicrystal based on the model in Eq. (8). Parameters are $\epsilon_{p_x, p_y} = 1.58$, $\epsilon_{d_{x^2-y^2, xy}} = -0.42$, $V_{pp\sigma} = -1.783$, $V_{pp\pi} = -0.299$, $V_{pd\sigma} = 0.359$, $V_{pd\pi} = 0.280$, $V_{dd\sigma} = 0.299$, $V_{dd\pi} = 0.257$, $V_{dd\delta} = 0.537$ eV. (a) Energy spectrum of the quasicrystal containing 1168 sites with OBC or twisted boundary condition (TBC). Insert shows 8 corner states (highlighted by red stars) in the bulk gap. (b) Spatial distribution of the in-gap corner states [red stars in (a)]. (c) The distribution of local Euler markers $e(\mathbf{r})$ in the quasicrystal with OBC.

190 We further check the effect of lattice size and different boundary conditions on the \mathbf{r} -
 191 space Euler number, as shown in Fig. 1(d). All calculated \mathbf{r} -space Euler numbers converge

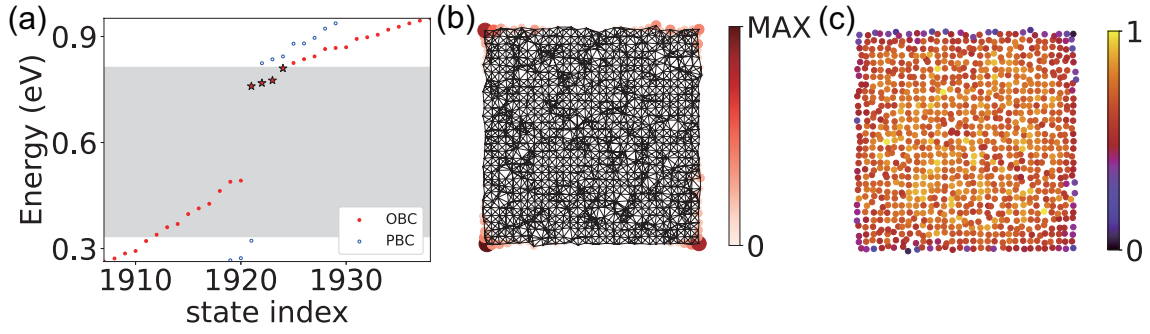


Figure 3: Fragile topological state characterized by $e = 1$ in the amorphous square lattice based on the model in Eq. (8). Each atom is assigned with a random displacement following the Gaussian distribution with standard deviation $\sigma = 0.2$. Parameters are $L=31$, $\epsilon_{p_x,p_y} = 1.58$, $\epsilon_{d_x^2-y^2,x_y} = -0.42$, $V_{pp\sigma}=-0.565$, $V_{pp\pi}=-0.044$, $V_{pd\sigma}=0.773$, $V_{pd\pi}=0.335$, $V_{dd\sigma}=0.444$, $V_{dd\pi}=0.224$, $V_{dd\delta}=0.659$ eV. (a) Energy spectrum of the amorphous square lattice with PBC and OBC. Four corner states in the gap are highlighted by red stars. (b) Spatial distribution of the corner states [red stars in (a)]. (c) The distribution of $e(\mathbf{r})$ for the amorphous system with OBC.

192 to the limit of 1 with different rates by increasing the lattice size, demonstrating the faithful
 193 formalism of the Euler number. Importantly, the OBC results exhibit a deviation from PBC due
 194 to the presence of open boundaries, but this difference can be diminished by increasing lattice
 195 size (see appendix I.4).

196 This suggests that the \mathbf{r} -space formula remains reliable regardless of the boundary condi-
 197 tions, which is notably different from the Chern number.

198 It is also noted that the disordered case converges much slower than the pristine PBC case.
 199 Because the disordered system is close to the critical point, the energy gap reduces signifi-
 200 cantly and the correlation length increases, which demands larger lattice sizes for accurate
 201 calculations of the real-space Euler number⁰. Our results show that the \mathbf{r} -space Euler number
 202 equals the exact one within a correction of order $\mathcal{O}(1/(L\Delta E))$ for systems with lattice size L
 203 and energy gap ΔE , which resembles the case of Bott index and Chern number [14].

204 6 Fragile topology in quasicrystals and amorphous lattices

205 As an application of our proposed \mathbf{r} -space formula, we explore the Euler topology in qua-
 206 sicrystals and amorphous lattices. Specifically, we consider the 2D Ammann-Beenker-tiling
 207 quasicrystal, which possesses 8-fold rotational symmetry but lacks translational symmetry. In
 208 the finite octagonal quasicrystal sample with open boundary conditions (OBC), 8 degenerate
 209 states emerge within the bulk gap region (grey area), as shown in Fig. 2(a). The bulk gap
 210 estimation utilizes a twisted boundary condition (TBC) to preserve octagonal symmetry and
 211 eliminate boundary effects (see appendix H.4). We plot the spatial distribution of these in-gap
 212 states [see Fig. 2(b)], and find that they are well localized at 8 corners of the octagonal qua-
 213 sicrystal, implying its feature of higher-order topology. We also examine the local Euler marker
 214 distribution in the finite quasicrystal sample, as depicted in Fig. 2(c). The plot confirms that
 215 the local Euler markers $e(\mathbf{r})$ closely match the expected value of 1 within the bulk but deviate
 216 at the edges. As expected, the average of $e(\mathbf{r})$ over the entire finite sample does not vanish but
 217 yields $e \approx 1$, verifying the nontrivial Euler topology of the quasicrystal.

218 We further study a finite amorphous lattice constructed by assigning random site displace-
 219 ments away from their equilibrium position in an initial square lattice. Consequently, all spatial

220 symmetries are broken, including \mathcal{P} or \mathcal{C}_{2z} demanded by \mathcal{I}_{ST} symmetry for real Bloch states in
 221 periodic crystals. Nevertheless, for the spinless model (8) in any amorphous lattice with OBC,
 222 it is always possible to choose a real gauge so that both the Hamiltonian and eigenstates can
 223 be taken real (see appendix G). This implies that the \mathbf{r} -space Euler number is still applicable to
 224 identify its Euler topology. As shown in Fig. 3(a), the energy spectrum of the finite amorphous
 225 lattice with OBC exhibits 4 corner states at the Fermi level in the bulk gap estimated using
 226 artificial PBC (grey area). The spatial distribution of these states supports that they are indeed
 227 localized at 4 corners of the finite sample [see Fig. 3(b)]. As shown in Fig. 3(c), local Euler
 228 markers $e(\mathbf{r})$ are dominated in the internal area but tend to vanish at the boundary of the fi-
 229 nite amorphous sample. The sum of $e(\mathbf{r})$ over the entirety of the finite sample yields a nonzero
 230 Euler number which is expected to converge to the quantized value of 1 with increasing lattice
 231 size.

232 7 Conclusion

233 We have proposed an explicit real-space formula for the Euler number to identify the fragile
 234 topological phases in both crystalline and noncrystalline systems whose wave functions are
 235 real. Specifically, the local Euler marker $e(\mathbf{r})$ whose macroscopic average coincides with the
 236 Euler number e , is introduced to characterize the topological order in real space. Notably,
 237 this applies equally well to periodic and open boundary conditions. We have validated our
 238 expression by diagnosing the topological phase transition in crystals and disordered systems
 239 with \mathcal{PT} symmetry. Furthermore, we have also uncovered the topological Euler phases in
 240 quasicrystals and amorphous lattices without any spatial symmetry. Our work greatly extends
 241 the concept of real-space topological markers to topological states in real Hilbert space and
 242 would hopefully inspire future exploration in more topological characteristic classes in real
 243 space.

244 Acknowledgements

245 We thank Guo Chuan Thiang for the valuable discussions.

246 **Author contributions** D.L. and C.W. contributed equally to this work.

247 **Funding information** This work is supported by the National Key R&D Program of China
 248 (Grant No. 2021YFA1401600) and the National Natural Science Foundation of China (Grant
 249 No. 12074006). The computational resources were supported by the high-performance com-
 250 puting platform of Peking University.

251 A Orientability of our models

252 In this section, we examine the orientability of our models. The Euler class $\epsilon(\mathcal{F})$ is defined as

$$\epsilon(\mathcal{F}) = \frac{1}{2\pi} \text{Pf}(\mathcal{F}), \quad (\text{A.1})$$

253 where Pf denotes the Pfaffian acting on the curvature matrix \mathcal{F} . Under the basis transformation
254 O , the Euler class acquires an additional factor $\det(O)$, as shown below:

$$\begin{aligned}\epsilon(\mathcal{F}) &\rightarrow \epsilon(O^{-1}\mathcal{F}O), \\ &= \frac{1}{2\pi}\text{Pf}(O^{-1}\mathcal{F}O), \\ &= \frac{1}{2\pi}\text{Pf}(O^T\mathcal{F}O),\end{aligned}\tag{A.2}$$

255 where the last equality originates from the orthonormality property of the real wave functions,
256 which means $O^{-1} = O^T$. It's worth noting that for a $2n \times 2n$ skew-symmetric matrix A and an
257 arbitrary $2n \times 2n$ matrix B , the Pfaffian satisfies the identity $\text{Pf}(B^T A B) = \text{Pf}(A)\det(B)$. There-
258 fore, since the curvature matrix \mathcal{F} is skew-symmetric, we can simplify the expression further
259 as:

$$\begin{aligned}\epsilon(\mathcal{F}) &\rightarrow \frac{1}{2\pi}\text{Pf}(\mathcal{F})\det(O), \\ &= \epsilon(\mathcal{F})\det(O).\end{aligned}\tag{A.3}$$

260 For the Euler class $\epsilon(\mathcal{F})$ to be a characteristic class, it must remain invariant under any bas-
261 is transformation. Therefore, a certain transformation matrix O with $\det(O) = 1$ is essential.
262 Since O is the transformation matrix between orthonormal basis, it naturally satisfies the con-
263 dition $|\det(O)|=1$. Thus, system orientability is necessary to prevent $\det(O) = -1$ and ensure
264 the invariance of the Euler class.

265 In fact, the orientability of the Brillouin zone is determined by the first Stiefel-Whitney
266 class w_1 , which is the total Berry phase of the occupied states over the Brillouin zone [45].
267 Because the Chern number of a time-reversal symmetric system is always trivial, a complex
268 smooth gauge can be found in this system. Given a Berry connection A that satisfies $\mathcal{F} = dA$
269 in this gauge, we have

$$w_1|_C = \frac{1}{\pi} \oint_C d\mathbf{k} \cdot \text{Tr}A(\mathbf{k}).\tag{A.4}$$

270 Therefore, our models are easily confirmed to be orientable with a trivial $w_1 = 0$, allowing us
271 to proceed with our discussion on the Euler class and the second Stiefel-Whitney class.

272 B Derivation of Eq. (4) in the main text

273 In this section, we derive Eq. (4) in the main text, beginning with the relation between the
274 Chern and Euler class in a two-dimensional system. Specifically, there is a correspondence
275 between the first Chern class c_1 and the Euler class ϵ :

$$c_1(\mathcal{F}_\mathbb{C}) = \epsilon(\mathcal{F}),\tag{B.1}$$

276 where $\mathcal{F}_\mathbb{C}$ is the curvature over a complex number field, isomorphic to \mathcal{F} over a real number
277 field through an isomorphism $\mathbb{C} \cong \mathbb{R} \oplus \mathbb{R}$. In particular, for a system with two occupied bands
278 ($N_{\text{occ}} = 2$), we can construct a complex Bloch state

$$|u\rangle = \frac{1}{\sqrt{2}}(|u_1\rangle + i|u_2\rangle),\tag{B.2}$$

279 where $|u_n\rangle$ ($n = 1, 2$) represents the cell-periodic part of the n -th occupied Bloch state $|\psi_n(\mathbf{k})\rangle$.
280 Note that for brevity, we omit the explicit dependence of \mathbf{k} in this section for $|u_n(\mathbf{k})\rangle$, $|u(\mathbf{k})\rangle$,

281 and the projection operator $\tilde{P}(\mathbf{k})$. Based on the complex Bloch states, the first Chern class is
 282 given by

$$c_1(\mathcal{F}_\mathbb{C}) = \frac{1}{2\pi i} \mathcal{F}_\mathbb{C} = \frac{1}{2\pi i} \langle \partial_{[k_x} u | \partial_{k_y]} u \rangle dk_x \wedge dk_y. \quad (\text{B.3})$$

283 This allows us to derive the expression of the Euler class from the first Chern class.

284 To begin with, we can express the first Chern number as a \mathbf{k} -space integral:

$$c_1 = \frac{1}{2\pi i} \int_{BZ} d^2\mathbf{k} \text{Tr}(\tilde{P} \partial_{[k_x} \tilde{P} \partial_{k_y]} \tilde{P}), \quad (\text{B.4})$$

285 where the integral is over the Brillouin zone (BZ) and $\tilde{P} = |u\rangle\langle u|$ is the projection operator,
 286 with its real and imaginary parts given by:

$$\text{Re}\tilde{P} = \frac{1}{2}(|u_1\rangle\langle u_1| + |u_2\rangle\langle u_2|) \quad (\text{B.5})$$

287 and

$$\text{Im}\tilde{P} = \frac{1}{2}(|u_2\rangle\langle u_1| - |u_1\rangle\langle u_2|). \quad (\text{B.6})$$

288 Using Eq. (B.2), we can rewrite Eq. (B.4) as

$$c_1 = \frac{1}{2\pi i} \int_{BZ} d^2\mathbf{k} \langle u | [\partial_{k_x} \tilde{P}, \partial_{k_y} \tilde{P}] | u \rangle, \quad (\text{B.7})$$

289 and then the Euler number is given by

$$\begin{aligned} e &= \frac{1}{4\pi i} \int_{BZ} d^2\mathbf{k} \langle u_1 | [\partial_{k_x} \tilde{P}, \partial_{k_y} \tilde{P}] | u_1 \rangle + \frac{1}{4\pi i} \int_{BZ} d^2\mathbf{k} \langle u_2 | [\partial_{k_x} \tilde{P}, \partial_{k_y} \tilde{P}] | u_2 \rangle \\ &+ \frac{1}{4\pi} \int_{BZ} d^2\mathbf{k} \langle u_1 | [\partial_{k_x} \tilde{P}, \partial_{k_y} \tilde{P}] | u_2 \rangle - \frac{1}{4\pi} \int_{BZ} d^2\mathbf{k} \langle u_2 | [\partial_{k_x} \tilde{P}, \partial_{k_y} \tilde{P}] | u_1 \rangle. \end{aligned} \quad (\text{B.8})$$

290 To keep the Euler number e real, we can simplify the operators $[\partial_{k_x} \tilde{P}, \partial_{k_y} \tilde{P}]$ in Eq. (B.8) to

$$i[\partial_{k_x} \text{Re}\tilde{P}, \partial_{k_y} \text{Im}\tilde{P}] + i[\partial_{k_x} \text{Im}\tilde{P}, \partial_{k_y} \text{Re}\tilde{P}] \quad (\text{B.9})$$

291 for the first two terms and

$$[\partial_{k_x} \text{Re}\tilde{P}, \partial_{k_y} \text{Re}\tilde{P}] - [\partial_{k_x} \text{Im}\tilde{P}, \partial_{k_y} \text{Im}\tilde{P}] \quad (\text{B.10})$$

292 for the other terms. Since $\{|u_n\rangle\}$ are orthonormal, we have the following identities:

$$\langle u_n | u_m \rangle = \delta_{n,m} \quad (\text{B.11})$$

293 and

$$\langle u_n | \partial_{k_i} u_n \rangle = \frac{1}{2} \partial_{k_i} (\langle u_n | u_n \rangle) = 0. \quad (\text{B.12})$$

294 Therefore, we have

$$\begin{cases} \partial_{k_i} \text{Re}\tilde{P} | u_1 \rangle = \frac{1}{2} (|\partial_{k_i} u_1\rangle + |u_2\rangle \langle u_1 | \partial_{k_i} u_2 \rangle) \\ \partial_{k_i} \text{Re}\tilde{P} | u_2 \rangle = \frac{1}{2} (|\partial_{k_i} u_2\rangle - |u_1\rangle \langle u_1 | \partial_{k_i} u_2 \rangle) \\ \partial_{k_i} \text{Im}\tilde{P} | u_1 \rangle = \frac{1}{2} (|\partial_{k_i} u_2\rangle - |u_1\rangle \langle u_1 | \partial_{k_i} u_2 \rangle) = \partial_{k_i} \text{Re}\tilde{P} | u_2 \rangle \\ \partial_{k_i} \text{Im}\tilde{P} | u_2 \rangle = -\frac{1}{2} (|\partial_{k_i} u_1\rangle + |u_2\rangle \langle u_1 | \partial_{k_i} u_2 \rangle) = -\partial_{k_i} \text{Re}\tilde{P} | u_1 \rangle, \end{cases} \quad (\text{B.13})$$

295 with k_i denoting k_x or k_y . Since $\text{Re}\tilde{P}$ is a Hermitian operator and $\text{Im}\tilde{P}$ is an anti-Hermitian
 296 operator, we have:

$$\langle u_n | \partial_{k_i} \text{Re}\tilde{P} = (\partial_{k_i} \text{Re}\tilde{P} | u_n \rangle)^\dagger \quad (\text{B.14})$$

297 and

$$-\langle u_n | \partial_{k_i} \text{Im}\tilde{P} = (\partial_{k_i} \text{Im}\tilde{P} | u_n \rangle)^\dagger, \quad (\text{B.15})$$

298 where the additional minus sign in Eq. (B.15) can be canceled by the minus sign in the com-
 299 mutators in Eq. (B.9) and Eq. (B.10).

300 Therefore, the first term in Eq. (B.8) is

$$\begin{aligned} & \frac{1}{4\pi i} \int_{BZ} d^2\mathbf{k} \langle u_1 | [\partial_{k_x} \tilde{P}, \partial_{k_y} \tilde{P}] | u_1 \rangle \\ &= \frac{1}{4\pi} \int_{BZ} d^2\mathbf{k} \langle u_1 | ([\partial_{k_x} \text{Re}\tilde{P}, \partial_{k_y} \text{Im}\tilde{P}] + [\partial_{k_x} \text{Im}\tilde{P}, \partial_{k_y} \text{Re}\tilde{P}]) | u_1 \rangle \\ &= \frac{1}{2\pi} \int_{BZ} d^2\mathbf{k} (\langle u_1 | \partial_{k_x} \text{Re}\tilde{P} \partial_{k_y} \text{Im}\tilde{P} | u_1 \rangle - \langle u_1 | \partial_{k_y} \text{Re}\tilde{P} \partial_{k_x} \text{Im}\tilde{P} | u_1 \rangle) \\ &= \frac{1}{2\pi} \int_{BZ} d^2\mathbf{k} (\langle u_1 | \partial_{k_x} \text{Re}\tilde{P} \partial_{k_y} \text{Re}\tilde{P} | u_2 \rangle - \langle u_1 | \partial_{k_y} \text{Re}\tilde{P} \partial_{k_x} \text{Re}\tilde{P} | u_2 \rangle) \\ &= \frac{1}{2\pi} \int_{BZ} d^2\mathbf{k} \langle u_1 | [\partial_{k_x} \text{Re}\tilde{P}, \partial_{k_y} \text{Re}\tilde{P}] | u_2 \rangle. \end{aligned} \quad (\text{B.16})$$

301 The analysis of the second term in Eq. (B.8) is similar, with the only difference being an addi-
 302 tional minus sign from Eq. (B.15) as

$$\begin{aligned} & \frac{1}{4\pi i} \int_{BZ} d^2\mathbf{k} \langle u_2 | [\partial_{k_x} \tilde{P}, \partial_{k_y} \tilde{P}] | u_2 \rangle \\ &= -\frac{1}{2\pi} \int_{BZ} d^2\mathbf{k} \langle u_2 | \partial_{[k_x} \text{Re}\tilde{P} \partial_{k_y]} \text{Re}\tilde{P} | u_1 \rangle \\ &= \frac{1}{2\pi} \int_{BZ} d^2\mathbf{k} \langle u_1 | [\partial_{k_x} \text{Re}\tilde{P}, \partial_{k_y} \text{Re}\tilde{P}] | u_2 \rangle, \end{aligned} \quad (\text{B.17})$$

303 where the last equality holds due to the Hermiticity of $\text{Re}\tilde{P}$ and the reality of $|u_n\rangle$. Now, let's
 304 consider the third term in Eq. (B.8), which is

$$\begin{aligned} & \frac{1}{4\pi} \int_{BZ} d^2\mathbf{k} \langle u_1 | [\partial_{k_x} \tilde{P}, \partial_{k_y} \tilde{P}] | u_2 \rangle \\ &= \frac{1}{4\pi} \int_{BZ} d^2\mathbf{k} (\langle u_1 | [\partial_{k_x} \text{Re}\tilde{P}, \partial_{k_y} \text{Re}\tilde{P}] | u_2 \rangle - \langle u_1 | [\partial_{k_x} \text{Im}\tilde{P}, \partial_{k_y} \text{Im}\tilde{P}] | u_2 \rangle) \\ &= \frac{1}{4\pi} \int_{BZ} d^2\mathbf{k} (\langle u_1 | [\partial_{k_x} \text{Re}\tilde{P}, \partial_{k_y} \text{Re}\tilde{P}] | u_2 \rangle - \langle u_2 | [\partial_{k_x} \text{Re}\tilde{P}, \partial_{k_y} \text{Re}\tilde{P}] | u_1 \rangle) \\ &= \frac{1}{2\pi} \int_{BZ} d^2\mathbf{k} \langle u_1 | [\partial_{k_x} \text{Re}\tilde{P}, \partial_{k_y} \text{Re}\tilde{P}] | u_2 \rangle. \end{aligned} \quad (\text{B.18})$$

305 Likewise, the final term in Eq. (B.8) can be expressed as:

$$\frac{1}{2\pi} \int_{BZ} d^2\mathbf{k} \langle u_1 | [\partial_{k_x} \text{Re}\tilde{P}, \partial_{k_y} \text{Re}\tilde{P}] | u_2 \rangle, \quad (\text{B.19})$$

306 due to the anti-symmetry of $|u_1\rangle$ and $|u_2\rangle$.

307 Therefore, Eq. (B.8) is now simplified to

$$e = \frac{2}{\pi} \int_{BZ} d^2\mathbf{k} \langle u_1 | [\partial_{k_x} \text{Re}\tilde{P}, \partial_{k_y} \text{Re}\tilde{P}] | u_2 \rangle. \quad (\text{B.20})$$

308 The relevant operator in the above expression is $\text{Re}\tilde{P}$. By introducing the real projector

$$\hat{P} := \sum_n^{\text{occ}} |u_n\rangle \langle u_n|, \quad (\text{B.21})$$

309 we obtain the following identities:

$$\hat{P} = 2\text{Re}\tilde{P} \quad (\text{B.22})$$

310 and

$$\hat{P}|u_n\rangle = |u_n\rangle. \quad (\text{B.23})$$

311 Thus, the formula Eq. (B.20) of the Euler number can be further expressed as:

$$e = \frac{1}{2\pi} \int_{BZ} d^2\mathbf{k} \langle u_1 | \hat{P} [\partial_{k_x} \hat{P}, \partial_{k_y} \hat{P}] | u_2 \rangle. \quad (\text{B.24})$$

312 Due to the symmetry of $k_{x,y}$ and $|u_{1,2}\rangle$, the final form of the Euler number in \mathbf{k} -space is

$$e = \frac{1}{2\pi} \int_{BZ} d^2\mathbf{k} \text{Pf}_{\text{occ}}(\hat{P} [\partial_{k_x} \hat{P}, \partial_{k_y} \hat{P}]), \quad (\text{B.25})$$

313 which is nothing but the Eq. (4) in the main text. Here Pf_{occ} denotes the Pfaffian taken over
314 the occupied subspace. To be specific, in the eigenbasis, a general matrix \mathbf{M} can be represented
315 as a block matrix

$$\mathbf{M} = \begin{pmatrix} M_1 & M_2 \\ M_3 & M_{\text{occ}} \end{pmatrix}, \quad (\text{B.26})$$

316 where M_{occ} is the submatrix of \mathbf{M} constructed by occupied eigenbasis. Therefore, Pf_{occ} , which
317 is the Pfaffian taken over the occupied subspace, is defined as

$$\text{Pf}_{\text{occ}}(M) := \text{Pf}(M_{\text{occ}}). \quad (\text{B.27})$$

318 C Derivation of Eq. (6) in the main text

319 In this section, we derive Eq. (6) in the main text, demonstrating its equivalence to Eq. (4) in
320 the main text under translational invariance.

321 Before proceeding, we first introduce some basic basis for the operators used in the deriva-
322 tion. Firstly, we use a \mathbf{k} -mesh form instead of the continuous form of the system. In real space,
323 the Hamiltonian \hat{H} is constructed under a certain initial local basis $\{|\alpha\mathbf{r}\rangle\}$ with $|\alpha\mathbf{r}\rangle = |\mathbf{r}\rangle \otimes |\alpha\rangle$,
324 i.e.,

$$\hat{H} = \sum_{\alpha'\mathbf{r}', \alpha''\mathbf{r}''} |\alpha'\mathbf{r}'\rangle \langle \alpha''\mathbf{r}'' | H_{\alpha'\mathbf{r}', \alpha''\mathbf{r}''}, \quad (\text{C.1})$$

325 where α and \mathbf{r} denote the internal and coordinate index, respectively. In \mathbf{k} space, it is con-
326 venient to use the Bloch basis $\{|\psi_n(\mathbf{k})\rangle\}$ satisfying $|\psi_n(\mathbf{k})\rangle = |\mathbf{k}\rangle \otimes |u_n(\mathbf{k})\rangle$ where $\{|\mathbf{k}\rangle\}$ is the

327 plane wave basis with $\langle \mathbf{r} | \mathbf{k} \rangle = \frac{1}{\sqrt{A}} e^{-i\mathbf{k} \cdot \mathbf{r}}$ and $A = L_x L_y$ being the area of the system. We can
 328 thus construct the \mathbf{k} -space Hamiltonian $\hat{H}(\mathbf{k})$ as

$$\begin{aligned} \hat{H}(\mathbf{k}) &= \langle \mathbf{k} | \hat{H} | \mathbf{k} \rangle \\ &= \sum_{\alpha', \alpha''} |\alpha'(\mathbf{k})\rangle \langle \alpha''(\mathbf{k})| H_{\alpha', \alpha''}(\mathbf{k}) \\ &= \sum_n |u_n(\mathbf{k})\rangle \langle u_n(\mathbf{k})| E_n(\mathbf{k}). \end{aligned} \quad (\text{C.2})$$

329 Here, the second equality is established due to the translational invariance of the Hamiltonian.
 330 Additionally, the cell-periodic Bloch basis $\{|u_n(\mathbf{k})\rangle\}$ is the eigenbasis of $\hat{H}(\mathbf{k})$.

331 Then, we can define the projection operator acting on different basis sets as [85]

$$\begin{aligned} \hat{P} &= \sum_{n\mathbf{k}}^{\text{occ}} |\psi_n(\mathbf{k})\rangle \langle \psi_n(\mathbf{k})| \\ &= \sum_{\mathbf{k}} |\mathbf{k}\rangle \langle \mathbf{k}| \sum_n^{\text{occ}} |u_n(\mathbf{k})\rangle \langle u_n(\mathbf{k})| \\ &= \sum_{\mathbf{k}} |\mathbf{k}\rangle \langle \mathbf{k}| \sum_{\alpha', \alpha''} |\alpha'(\mathbf{k})\rangle \langle \alpha''(\mathbf{k})| P_{\alpha', \alpha''}(\mathbf{k}) \\ &= \sum_{\mathbf{k}, \alpha', \alpha''} |\alpha' \mathbf{k}\rangle \langle \alpha'' \mathbf{k}| P_{\mathbf{k}, \alpha', \alpha''} \\ &= \sum_{\alpha' \mathbf{r}', \alpha'' \mathbf{r}''} |\alpha' \mathbf{r}'\rangle \langle \alpha'' \mathbf{r}''| P_{\alpha' \mathbf{r}', \alpha'' \mathbf{r}''}. \end{aligned} \quad (\text{C.3})$$

332 So the \mathbf{k} -space projector $\hat{P}(\mathbf{k}) = \sum_n^{\text{occ}} |u_n(\mathbf{k})\rangle \langle u_n(\mathbf{k})|$ can be explicitly represented as a matrix
 333 $P(\mathbf{k})$ under basis $\{|\alpha(\mathbf{k})\rangle\}$. For convenience, we can create a new projection matrix $P_{\mathbf{k}}$, which
 334 is a quasi-diagonal matrix with $P(\mathbf{k})$ as diagonal blocks. In fact, $P_{\mathbf{k}}$ represents \hat{P} under basis
 335 set $\{|\alpha \mathbf{k}\rangle\}$ and is related to P under basis set $\{|\alpha \mathbf{r}\rangle\}$ via a unitary basis transformation. Specif-
 336 ically, we can construct a transformation matrix $U_{\mathbf{k}, \mathbf{r}}$ with the entries as $\langle \mathbf{r} | \mathbf{k} \rangle$ to denote this
 337 basis transformation. Notice that $U_{\mathbf{k}, \mathbf{r}}$ is indeed a unitary matrix in the thermodynamic limit
 338 $A \rightarrow \infty$. Therefore, we can obtain the \mathbf{r} -space projection matrix P under the local basis by
 339 transforming $P_{\mathbf{k}}$ using the the transformation:

$$P_{\mathbf{k}} = U_{\mathbf{k}, \mathbf{r}} P U_{\mathbf{k}, \mathbf{r}}^\dagger. \quad (\text{C.4})$$

340 Now we start to derive Eq. (6). Since the integral is now discretized as

$$\frac{A}{(2\pi)^2} \int_{BZ} d^2 \mathbf{k} \rightarrow \sum_{\mathbf{k}}, \quad (\text{C.5})$$

341 we can define its equivalent operation $\text{Tr}_{\mathbf{k}}$ acting on the block index \mathbf{k} of $P_{\mathbf{k}}$. Therefore, the
 342 \mathbf{k} -space Euler number can be expressed in the matrix form as

$$e = \frac{2\pi}{A} \text{Tr}_{\mathbf{k}} \text{Pf}_{\text{occ}}(P_{\mathbf{k}} [\partial_{k_x} P_{\mathbf{k}}, \partial_{k_y} P_{\mathbf{k}}]). \quad (\text{C.6})$$

343 In a translational invariant system, the \mathbf{k} space and the coordinate space can be connected
 344 via the Fourier transformation. Therefore, we have

$$\begin{aligned} \partial_{k_x} \hat{P}(\mathbf{k}) &\rightarrow \frac{1}{\delta k_x} (P_{\mathbf{k} + \delta \mathbf{k}} - P_{\mathbf{k}}) \\ &= \frac{1}{\delta k_x} (U_{\mathbf{k} + \delta \mathbf{k}, \mathbf{r}} P U_{\mathbf{k} + \delta \mathbf{k}, \mathbf{r}}^\dagger - U_{\mathbf{k}, \mathbf{r}} P U_{\mathbf{k}, \mathbf{r}}^\dagger) \\ &= U_{\mathbf{k}, \mathbf{r}} \left[\frac{1}{\delta k_x} (U_{\delta \mathbf{k}, \mathbf{r}} P U_{\delta \mathbf{k}, \mathbf{r}}^\dagger - P) \right] U_{\mathbf{k}, \mathbf{r}}^\dagger, \end{aligned} \quad (\text{C.7})$$

345 where $\delta \mathbf{k} = (\delta k_x, 0)$. If we set $\delta k_x = \frac{2\pi}{L_x}$, then $U_{\delta \mathbf{k}, r}$ is just the unitary position matrix
 346 $U = e^{i\frac{2\pi}{L_x}X}$. Similarly, the relation applies to the other unitary position matrix $V = e^{i\frac{2\pi}{L_y}Y}$.
 347 Based on these quantities defined in \mathbf{r} space, the Euler number in Eq. (C.6) can be reformulated as
 348

$$\begin{aligned} e &= \frac{1}{2\pi} \text{Pf}_{\text{occ}} \sum_{\mathbf{k}} U_{\mathbf{k}, r} P [U P U^\dagger, V P V^\dagger] U_{\mathbf{k}, r}^\dagger \\ &= \frac{1}{2\pi} \text{Pf}_{\text{occ}} \text{Tr}(U_{\mathbf{k}, r} P [U P U^\dagger, V P V^\dagger] U_{\mathbf{k}, r}^\dagger) \\ &= \frac{1}{2\pi} \text{Pf}_{\text{occ}} \text{Tr}(P [U P U^\dagger, V P V^\dagger]), \end{aligned} \quad (\text{C.8})$$

349 where the last equation holds because of the invariant property of the trace under any unitary
 350 transformation. Since the trace and Pfaffian operations act on different individual subspaces,
 351 they are commutative as operators on the Wannier basis with $N_{\text{occ}} = 2$, which proves exactly
 352 the Eq. (6).

353 In principle, when δk_x is small enough, one can perform the Taylor expansion up to the
 354 first order

$$\frac{1}{\delta k_x} (U_{\delta \mathbf{k}, r} P U_{\delta \mathbf{k}, r}^\dagger - P) \approx i[X, P] \quad (\text{C.9})$$

355 to the right side of Eq. (C.7). However, for a \mathcal{PT} -symmetric system with real eigenbasis
 356 $\{|u_n(\mathbf{k})\}$, both the projection operator $P_{\mathbf{k}}$ and its derivative $\partial_{k_x} P_{\mathbf{k}}$ are supposed to be real-
 357 valued. The first-order expansion term $i[X, P]$, which deviates from the real field \mathbb{R} , should
 358 cancel with some other first-order terms (and higher-order terms may contribute significantly)
 359 to ensure the real-valued final expression. Therefore, the additional real-value limitation from
 360 the \mathcal{PT} symmetry necessitates the use of the unitary position matrix U instead of the usual
 361 position matrix X in our final expression of the \mathbf{r} -space Euler number. This is different from
 362 the case of the Chern number where the first-order expansion is applicable to yield a simplified
 363 \mathbf{r} -space formula in Ref. [11, 14].

364 D Numerical implementation of the real-space Euler number

365 In this section, we demonstrate the practical calculation of Eq. (6) in the main text. We begin
 366 by selecting a suitable basis for expressing the operators in the equation. Once this basis is
 367 established, we can straightforwardly apply trace and Pfaffian operations.

368 We initially work with a set of local coordinate space bases, from which we construct
 369 diagonal matrices representing the unitary position operators \hat{U} and \hat{V} . The projector \hat{P} is
 370 defined as

$$\mathbf{1}_{\text{occ}} = \begin{pmatrix} \mathbf{0} & \mathbf{0} \\ \mathbf{0} & \mathbf{1} \end{pmatrix} \quad (\text{D.1})$$

371 in the eigenbasis of the Hamiltonian, with eigenvalues arranged in descending order. Here, $\mathbf{0}$
 372 and $\mathbf{1}$ represent the null matrix and identity matrix, respectively.

373 To proceed, we diagonalize the Hamiltonian to obtain the eigenvalues and eigenvectors in
 374 the local basis. This allows us to create a unitary transformation matrix from the local basis to
 375 the eigenbasis of the system. In other words, we have

$$H = \Pi D \Pi^{-1}, \quad (\text{D.2})$$

376 where D is a diagonal matrix with the eigenvalues in descending order, and the columns of Π
 377 are the corresponding eigenvectors. Subsequently, we determine the explicit expression of the

378 projector \hat{P} through this unitary transformation of the basis, as follows:

$$P = \Pi \mathbf{1}_{occ} \Pi^{-1}. \quad (\text{D.3})$$

379 All operators are now represented in a unified local basis, simplifying the matrix calcula-
380 tions. To carry out the trace and Pfaffian operations, a basis transformation from the initial lo-
381 cal basis to a composite Wannier basis is required. This Wannier basis can be constructed from
382 the eigenbasis by minimizing the Marzari-Vanderbilt localization functional [84, 85]. Once we
383 have the transformation matrix Π from the eigenbasis to the local basis and S from the eigen-
384 basis to the composite Wannier basis, we can obtain the matrix form of the expression within
385 the brackets in Eq. (C.8):

$$M = S \Pi^{-1} P [U P U^\dagger, V P V^\dagger] \Pi S^{-1}. \quad (\text{D.4})$$

386 In this basis, the matrix entries are denoted as $M_{n'n'', r'r''}$. Then the trace operation simply
387 involves summing over the coordinate index r , expressed as

$$\text{Tr} := \sum_{r', r''} \delta_{r', r''}. \quad (\text{D.5})$$

388 Finally, the r -space Euler number can be obtained by performing the Pfaffian over occupied
389 space as ¹

$$\text{Pf}_{occ}(\text{Tr}M) = \text{Pf}(\text{Tr}M)_{occ}. \quad (\text{D.6})$$

390 The final step of basis transformation is crucial for accurately calculating the r -space Euler
391 number. This transformation is necessary because only on the Wannier basis can we effec-
392 tively separate the total space into internal and coordinate spaces. When using a set of local
393 basis functions with high localization properties, such as atomic orbitals, the hopping terms
394 of the Hamiltonian naturally mix the coordinate and internal spaces. As a result, it becomes
395 challenging to distinguish the occupied subspace within the internal space, making it difficult
396 to perform the Pfaffian operation using this basis. On the other hand, the eigenbasis of the
397 Hamiltonian is not suitable either. Although it allows for the easy identification of the occupied
398 subspace, this highly delocalized basis presents difficulties in aligning it in a meaningful way
399 to perform the trace and Pfaffian operations correctly.

400 E The distinction between the real-space Chern and Euler num- 401 bers

402 In this section, we give some remarks on the distinction between the real-space Chern and
403 Euler numbers. First, the analysis we've conducted can be directly applied to the Chern class,
404 and the resultant r -space expression is nothing but the Bott index,

$$\text{Bott}(\hat{U}, \hat{V}) = \frac{1}{2\pi} \text{ImTr} \log(\hat{U} \hat{V} \hat{U}^{-1} \hat{V}^{-1}), \quad (\text{E.1})$$

405 with $\hat{U} = \hat{P} \exp(2\pi i \hat{X}/L_x) \hat{P}$ and $\hat{V} = \hat{P} \exp(2\pi i \hat{Y}/L_y) \hat{P}$, which measures the commutativity
406 of the position operators and offers an identical topological classification as the Chern number
407 [14, 15]. The Bott index can be further simplified by applying the Taylor expansion of the
408 unitary position operator up to the first order, which yields the conventional r -space formula
409 of the Chern number in Ref. [11, 14]

$$c_1 = \frac{4\pi}{L^2} \text{ImTr}'(\hat{P}[\hat{X}, \hat{P}][\hat{Y}, \hat{P}]), \quad (\text{E.2})$$

¹The package code is available at <https://github.com/li-dexin-phy/realeulernum>.

410 where \hat{X}, \hat{Y} are the usual position operators and Tr' is the usual trace operation acting on the
 411 whole space, distinguished from the aforementioned Tr acting on coordinate subspace only.

412 However, there are significant differences between the r -space formulation of the Euler
 413 defined in Eq. (6) and Chern number. This distinction arises because the Chern and Euler
 414 classes are defined by distinct invariant polynomials of the curvature [82]. When calculating
 415 the Chern number in real space, the trace operation is applied to both the internal and coordi-
 416 nate spaces, resulting in a simplified expression with only a single trace operation. In contrast,
 417 when calculating the r -space Euler number, it becomes essential to distinguish between the
 418 coordinate space and the internal space, which requires trace and Pfaffian operations, respec-
 419 tively.

420 The discussion is more clear in the frame of matrix form. For any operator of the form
 421 $M = \begin{pmatrix} \mathbf{0} & \mathbf{0} \\ \mathbf{0} & M_{occ} \end{pmatrix}$ with $\mathbf{0}$ being the null matrix, the relation $\text{Tr}_{occ} M := \text{Tr} M_{occ} = \text{Tr} \begin{pmatrix} \mathbf{0} & \mathbf{0} \\ \mathbf{0} & M_{occ} \end{pmatrix}$
 422 always holds. This is because the trace operation is just to sum over the diagonal of the matrix
 423 M , which means that the trace over a specific matrix is equal to the trace over the direct sum
 424 of this matrix and any null matrix. Therefore, we can safely consider the whole space without
 425 further restriction in the occupied space and the result remains the same. However, the Pfaf-
 426 fian does not possess this property, i.e., $\text{Pf} \begin{pmatrix} \mathbf{0} & \mathbf{0} \\ \mathbf{0} & M_{occ} \end{pmatrix} = \mathbf{0}$. What's more, the ordering of the
 427 basis does not matter for the trace since the sum operation is commutative, while the order-
 428 ing is crucial in the definition of the Pfaffian. Therefore, although a single Tr' is enough for
 429 calculating the r -space Chern number, it is important to find such a basis that can distinguish
 430 the internal space from the coordinate space.

431 This distinction is already evident in the k -space scenario. In a periodic lattice, the Bloch
 432 states $\{|\psi_n(\mathbf{k})\rangle\}$ can be transformed into Wannier states, which inherently distinguish the
 433 coordinate space from the internal space. Specifically, in such a translational invariant system,
 434 the Hamiltonian commutes with the translation operator, indicating a common eigenvalue for
 435 both operators. Since the energy index n and \mathbf{k} denoting quasi-momentum are independent
 436 of each other, it is straightforward to change the basis of \mathbf{k} via the Fourier transformation
 437 to r without mixture from n and derive the Wannier basis. However, if the system lacks
 438 translational invariance, the usual Fourier transformation from Bloch states fails to generate
 439 Wannier states. Consequently, it becomes crucial to consider composite Wannier functions
 440 defined in real space via a unitary transformation from energy eigenstates, without imposing
 441 further restrictions.

442 Secondly, It is worth noting that there is a gauge freedom in the Wannier functions and the
 443 determination of the exponentially localized Wannier functions is significant [84]. The exist-
 444 ence of the nontrivial Euler number prohibits finding such a basis of Wannier functions, which
 445 means that in a space-time inversion symmetric two-dimensional system, the exponentially lo-
 446 calized Wannier functions can not be constructed in a phase with nontrivial Euler number [49].
 447 Nevertheless, this is not an obstacle to search for the required composite Wannier functions
 448 that are not exponentially localized [88].

449 F Averaging the local Euler marker in finite systems with OBC

450 In finite systems with OBC, a striking contrast emerges between the local Chern marker and the
 451 local Euler marker. While averaging the local Chern marker over such systems yields vanishing
 452 results, the same averaging process for the local Euler marker results in non-vanishing values.
 453 This disparity highlights a fundamental distinction between the Chern number and the Euler
 454 number when calculated in finite systems under OBC, as elaborated below.

455 To calculate the r -space Chern number c_1 in Eq. (E.2), we employ standard position op-
 456 erators \hat{X} and \hat{Y} to construct the operator $\hat{P}[\hat{X}, \hat{P}][\hat{Y}, \hat{P}]$. Notably, the imaginary part of this
 457 operator is directly proportional to c_1 when subjected to a trace operation [11, 14]:

$$c_1 \propto \text{ImTr}'(\hat{P}[\hat{X}, \hat{P}][\hat{Y}, \hat{P}]). \quad (\text{E.1})$$

458 Utilizing the transpose invariance and the cyclic property of the trace operation and consider-
 459 ing the symmetry of operators \hat{X} and \hat{Y} , we can rigorously demonstrate the vanishing of the
 460 r -space Chern number under OBC [14]:

$$\begin{aligned} c_1 &\propto \text{ImTr}'(\hat{P}[\hat{X}, \hat{P}][\hat{Y}, \hat{P}]) \\ &= \text{ImTr}'(\hat{P}(\hat{X}\hat{P} - \hat{P}\hat{X})(\hat{Y}\hat{P} - \hat{P}\hat{Y})) \\ &= \text{ImTr}'(\hat{P}\hat{X}\hat{P}\hat{Y}\hat{P} - \hat{P}\hat{X}\hat{P}^2\hat{Y} - \hat{P}^2\hat{X}\hat{Y}\hat{P} + \hat{P}^2\hat{X}\hat{P}\hat{Y}) \\ &= \text{ImTr}'(\hat{P}\hat{X}\hat{P}\hat{Y}\hat{P} - \hat{P}\hat{X}\hat{P}\hat{Y} - \hat{P}\hat{X}\hat{Y}\hat{P} + \hat{P}\hat{X}\hat{P}\hat{Y}) \\ &= \text{ImTr}'(\hat{P}\hat{X}\hat{P}\hat{Y}\hat{P} - \hat{P}\hat{X}\hat{Y}\hat{P}), \end{aligned} \quad (\text{E.2})$$

461 where we utilize the property of the projection operator, $\hat{P}^2 = \hat{P}$. Note that \hat{P} , \hat{X} and \hat{Y} are all
 462 Hermitian, we can further simplify c_1 by expanding the imaginary part as the subtract of the
 463 operator with its conjugate,

$$\begin{aligned} c_1 &\propto \frac{1}{2i}(\text{Tr}'(\hat{P}\hat{X}\hat{P}\hat{Y}\hat{P} - \hat{P}\hat{X}\hat{Y}\hat{P}) - \text{Tr}'(\hat{P}\hat{X}\hat{P}\hat{Y}\hat{P} - \hat{P}\hat{X}\hat{Y}\hat{P})^*) \\ &= \frac{1}{2i}(\text{Tr}'(\hat{P}\hat{X}\hat{P}\hat{Y}\hat{P} - \hat{P}\hat{X}\hat{Y}\hat{P}) - \text{Tr}'(\hat{P}\hat{X}\hat{P}\hat{Y}\hat{P} - \hat{P}\hat{X}\hat{Y}\hat{P})^\dagger) \\ &= \frac{1}{2i}(\text{Tr}'(\hat{P}\hat{X}\hat{P}\hat{Y}\hat{P} - \hat{P}\hat{X}\hat{Y}\hat{P}) - \text{Tr}'(\hat{P}\hat{Y}\hat{P}\hat{X}\hat{P} - \hat{P}\hat{Y}\hat{X}\hat{P})). \end{aligned} \quad (\text{E.3})$$

464 This relationship is established through the transpose invariance of the trace operation, i.e.,

$$\text{Tr}'\hat{A} = \text{Tr}'\hat{A}^\text{T}, \quad (\text{E.4})$$

465 which leads to

$$\text{ImTr}'\hat{A} = \frac{1}{2i}(\text{Tr}'\hat{A} - \text{Tr}'\hat{A}^*) = \frac{1}{2i}(\text{Tr}'\hat{A} - \text{Tr}'\hat{A}^\dagger). \quad (\text{E.5})$$

466 Then, using the well-known cyclic property of trace operation, i.e., for general matrices \hat{A} and
 467 \hat{B} , it is known that

$$\text{Tr}'(\hat{A}\hat{B}) = \text{Tr}'(\hat{B}\hat{A}), \quad (\text{E.6})$$

468 c_1 can be further simplified as

$$\begin{aligned} c_1 &\propto \frac{1}{2i}(\text{Tr}'(\hat{P}\hat{X}\hat{P}\hat{Y}\hat{P}) - \text{Tr}'(\hat{P}\hat{X}\hat{Y}\hat{P}) - \text{Tr}'(\hat{P}\hat{Y}\hat{P}\hat{X}\hat{P}) + \text{Tr}'(\hat{P}\hat{Y}\hat{X}\hat{P})) \\ &= \frac{1}{2i}(\text{Tr}'(\hat{X}\hat{P}\hat{Y}\hat{P}^2) - \text{Tr}'(\hat{X}\hat{P}^2\hat{Y}\hat{P}) - \text{Tr}'(\hat{X}\hat{Y}\hat{P}^2) + \text{Tr}'(\hat{Y}\hat{X}\hat{P}^2)) \\ &= \frac{1}{2i}(\text{Tr}'(\hat{X}\hat{P}\hat{Y}\hat{P}) - \text{Tr}'(\hat{X}\hat{P}\hat{Y}\hat{P}) - \text{Tr}'(\hat{X}\hat{Y}\hat{P}) + \text{Tr}'(\hat{Y}\hat{X}\hat{P})) \\ &= -\frac{1}{2i}\text{Tr}'(\hat{X}\hat{Y}\hat{P} - \hat{Y}\hat{X}\hat{P}) \\ &= -\frac{1}{2i}\text{Tr}'([\hat{X}, \hat{Y}]\hat{P}) \\ &= 0, \end{aligned} \quad (\text{E.7})$$

469 where we have used the the symmetry of operators \hat{X} and \hat{Y}

$$[\hat{X}, \hat{Y}] = 0. \quad (\text{E.8})$$

470 In summary, the vanishing of the r -space Chern number under OBC arises from a cancel-
 471 lation effect, driven by three key factors:

- 472 • Transpose invariance of the trace operation: $\text{Tr}'\hat{A} = \text{Tr}'\hat{A}^T$.
- 473 • Cyclic property of the trace operation: $\text{Tr}'(\hat{A}\hat{B}) = \text{Tr}'(\hat{B}\hat{A})$.
- 474 • Symmetry of standard position operators \hat{X} and \hat{Y} : $[\hat{X}, \hat{Y}] = 0$.

475 In contrast, calculating the r -space Euler number doesn't encounter a similar cancellation
 476 effect, primarily due to the distinct properties of the trace operation and the Pfaffian. First,
 477 the transpose invariance, which holds for the trace operation, does not apply to the Pfaffian.
 478 For a general skew-symmetric matrices \hat{A} , we have

$$\text{Pf}\hat{A}^T = \text{Pf}(-\hat{A}) = \pm \text{Pf}\hat{A}, \quad (\text{F9})$$

479 with the additional sign depending on N_{occ} . Second, unlike the trace operation, the Pfaffian
 480 lacks the necessary cyclic properties for straightforward cancellation,

$$\text{Pf}(\hat{A}\hat{B}) \neq \text{Pf}(\hat{B}\hat{A}). \quad (\text{F10})$$

481 To be more specific, we now defined a r -space quantity ζ with trace operation only as

$$\begin{aligned} \zeta &= \frac{1}{2\pi} \text{Tr}'(\hat{P}[\hat{P}_U, \hat{P}_V]) \\ &= \frac{1}{2\pi} \text{Tr}'(\hat{P}\hat{P}_U\hat{P}_V - \hat{P}\hat{P}_V\hat{P}_U) \end{aligned} \quad (\text{F11})$$

482 where $\hat{P}_U = \hat{U}\hat{P}\hat{U}^\dagger$ and $\hat{P}_V = \hat{V}\hat{P}\hat{V}^\dagger$ are defined analogous to the expression of r -space Euler
 483 number.

484 Since the projector \hat{P} is Hermitian and \hat{U}/\hat{V} are both unitary operators, it is easy to prove
 485 that both operators are Hermitian operators. In addition, we further express the unitary posi-
 486 tion operators \hat{U}^\dagger and \hat{V}^\dagger as

$$\begin{aligned} \hat{U}^\dagger = \hat{U}^{-1} &= \exp(2\pi i(-\hat{X})/L_x) = \hat{I}\hat{U}\hat{I} \\ \text{and } \hat{V}^\dagger = \hat{V}^{-1} &= \exp(2\pi i(-\hat{Y})/L_y) = \hat{I}\hat{V}\hat{I}. \end{aligned} \quad (\text{F12})$$

487 where \hat{I} is the inversion operator. And in \mathcal{PT} -symmetric system, the projector \hat{P} is invariant
 488 under such inversion.

489 Since both Hamiltonian \hat{H} and projector \hat{P} satisfy the reality condition, the operators share
 490 the transpose invariant property as

$$\begin{aligned} \hat{P}^T &= \hat{P}^{*\dagger} = \hat{P}^\dagger = \hat{P}, \\ \hat{U}^T &= \hat{U}, \\ \hat{V}^T &= \hat{V}, \\ \hat{P}_U^T &= \hat{U}^\dagger\hat{P}\hat{U}, \\ \text{and } \hat{P}_V^T &= \hat{V}^\dagger\hat{P}\hat{V}. \end{aligned} \quad (\text{F13})$$

491 Now we can obtain the equivalent form of the first term in Eq. (F11) as

$$\begin{aligned} \frac{1}{2\pi} \text{Tr}'(\hat{P}\hat{P}_U\hat{P}_V) &= \frac{1}{2\pi} \text{Tr}'(\hat{P}\hat{P}_U\hat{P}_V)^T = \frac{1}{2\pi} \text{Tr}'(\hat{P}_V^T\hat{P}_U^T\hat{P}) = \frac{1}{2\pi} \text{Tr}'((\hat{V}\hat{P}\hat{V}^\dagger)^T\hat{P}_U^T\hat{P}) \\ &= \frac{1}{2\pi} \text{Tr}'(\hat{V}^\dagger\hat{P}\hat{V}\hat{P}_U^T\hat{P}) = \frac{1}{2\pi} \text{Tr}'(\hat{I}\hat{V}\hat{I}\hat{P}\hat{I}\hat{V}^\dagger\hat{I}\hat{P}_U^T\hat{I}) = \frac{1}{2\pi} \text{Tr}'(\hat{I}\hat{P}_V\hat{I}\hat{P}_U^T\hat{I}) = \frac{1}{2\pi} \text{Tr}'(\hat{I}\hat{P}_V\hat{P}_U\hat{I}) \\ &= \frac{1}{2\pi} \text{Tr}'(\hat{P}\hat{P}_V\hat{P}_U), \end{aligned} \quad (\text{F14})$$

492 which is just the second term of Eq. (F11). Therefore, we prove that ζ is trivial. Again, we
 493 notice that Eq. (F4) and Eq. (F5) are used in the first and the last equality respectively.

494 However, in the case of r -space Euler number e , as we have already discussed via Eq. (F9)
 495 and Eq. (F10), such cancellation doesn't exist. Hence, it becomes possible to calculate the
 496 r -space Euler number under OBC.

497 **G Brief discussion of the reality condition in \mathcal{PT} -broken systems**

498 Although we focus on the \mathcal{PT} -symmetric system in the main text, it is not a constraint on
 499 calculating the \mathbf{r} -space Euler number. In \mathbf{k} space, since the time reversal \mathcal{T} can be consid-
 500 ered a conjugate operator combined with a unitary matrix and a sign flip of \mathbf{k} , a \mathcal{T} -invariant
 501 Hamiltonian $H(\mathbf{k})$ satisfies $H(\mathbf{k}) = \hat{T}H(\mathbf{k})\hat{T}^{-1} = H^*(-\mathbf{k})$ under a proper basis obtained from
 502 Takagi decomposition. Therefore, only in a few time-reversal invariant momenta with $\mathbf{k} = -\mathbf{k}$
 503 can we derive a real Hamiltonian. To keep the Hamiltonian real in the whole \mathbf{k} -space, an-
 504 other operator such as \mathcal{P} and \mathcal{C}_{2z} that can reverse the sign of \mathbf{k} is essential. However, in \mathbf{r}
 505 space, the time reversal \mathcal{T} no longer acts on the sign of \mathbf{k} . This means that the symmetry
 506 requirement for the reality condition is only the time reversal \mathcal{T} . Therefore, in a finite system
 507 with OBC lacking spatial symmetry, we can again obtain the necessary basis from the initial
 508 local basis via a transformation matrix given by the Takagi decomposition. Under the new
 509 basis, the Hamiltonian is real-valued. By solving the eigenvalue problem of the Hamiltonian
 510 in such basis, the transformation matrix constructed by all eigenfunctions of the Hamiltonian
 511 is real-valued as well. This is just the reality condition necessitated for the definition of the
 512 Euler class. Consequently, one can apply the real-space formula of the Euler number to any
 513 nonmagnetic aperiodic systems with open boundary, such as quasicrystals, and amorphous
 514 materials without any spatial symmetries.

515 **H Details of the model and method**

516 **H.1 Model**

517 All the calculations are performed based on the tight-binding Hamiltonian in Eq. (8). The
 518 hopping integral $t_{\mu\nu}(\mathbf{r}_{ij})$ follows the Slater-Koster parameterization which depends on the
 519 orbital type and the directional cosines of the intersite vector $\mathbf{r}_{ij} = \mathbf{r}_i - \mathbf{r}_j$. To be more specific,

520 the explicit expression of Slater-Koster parameterized hopping integral are listed:

$$\begin{aligned}
t_{p_x, p_x} &= l^2 V_{pp\sigma} + (1 - l^2) V_{pp\pi}, \\
t_{p_y, p_y} &= m^2 V_{pp\sigma} + (1 - m^2) V_{pp\pi}, \\
t_{p_x, p_y} &= lm(V_{pp\sigma} - V_{pp\pi}), \\
t_{d_{x^2-y^2}, d_{x^2-y^2}} &= \frac{3}{4} V_{dd\sigma} (l^2 - m^2)^2 + (l^2 + m^2 - (l^2 - m^2)^2) V_{dd\pi} + \frac{1}{4} (l^2 - m^2)^2 V_{dd\delta}, \\
t_{d_{xy}, d_{xy}} &= l^2 m^2 (3V_{dd\sigma} - 4V_{dd\pi} + V_{dd\delta}) + V_{dd\pi}, \\
t_{d_{xy}, d_{x^2-y^2}} &= \frac{3}{2} lm(l^2 - m^2) V_{dd\sigma} + 2lm(m^2 - l^2) V_{dd\pi} + \frac{1}{2} lm(l^2 - m^2) V_{dd\delta}, \\
t_{p_x, d_{x^2-y^2}} &= \frac{\sqrt{3}}{2} l(l^2 - m^2) V_{pd\sigma} + l(1 - l^2 + m^2) V_{pd\pi}, \\
t_{p_y, d_{x^2-y^2}} &= \frac{\sqrt{3}}{2} m(l^2 - m^2) V_{pd\sigma} - m(1 + l^2 - m^2) V_{pd\pi}, \\
t_{p_x, d_{xy}} &= \sqrt{3} l^2 m V_{pd\sigma} + (1 - 2l^2) m V_{pd\pi}, \\
t_{p_y, d_{xy}} &= \sqrt{3} l m^2 V_{pd\sigma} + (1 - 2m^2) l V_{pd\pi}, \\
t_{p_y, p_x} &= t_{p_x, p_y}, \\
t_{d_{x^2-y^2}, d_{xy}} &= t_{d_{xy}, d_{x^2-y^2}}, \\
t_{d_{x^2-y^2}, p_x} &= -t_{p_x, d_{x^2-y^2}}, \\
t_{d_{x^2-y^2}, p_y} &= -t_{p_y, d_{x^2-y^2}}, \\
t_{d_{xy}, p_x} &= -t_{p_x, d_{xy}}, \\
t_{d_{xy}, p_y} &= -t_{p_y, d_{xy}},
\end{aligned} \tag{H.1}$$

521 where $\hat{r}_{ij} = (l, m)$ is the unit direction vector. The hopping strength is chosen to have an
522 inverse-square decay with the distance as $t_{\mu\nu}(\mathbf{r}_{ij}) \propto |\mathbf{r}_{ij}|^{-2}$. We adopt the equilibrium inter-
523 atomic bond length as the unit length a of the systems, which is the lattice constant for the
524 perfect square lattice and the side length of basic building blocks (square and rhombus) for
525 the Ammann-Beenker-tiling quasicrystals. In numerical calculations, we set the unit length of
526 the system $a = 1$ for simplicity.

527 We consider a 2D square lattice with a band inversion at the Γ -point in \mathbf{k} -space between
528 degenerate $p_{x,y}$ and $d_{x^2-y^2, xy}$ orbitals, as shown in Fig. 1(a). In real space, we investigate
529 $L \times L$ supercells of the square lattice with periodic boundary condition (PBC) or open boundary
530 condition (OBC). For convenience, we choose the lattice size L to be an odd integer, which
531 allows the supercell to possess an inversion center located at its central site.

532 H.2 Disorder of on-site energy

533 The tight-binding Hamiltonian with the onsite disorder is under our consideration as well.
534 Therefore, we introduce a disorder term to the Hamiltonian H as

$$H(\{\lambda_i\}) = H + \sum_{i\mu} \lambda_i c_{i\mu}^\dagger c_{i\mu}, \tag{H.2}$$

535 where $\{\lambda_i\}$ is a set of random on-site energy added to one-half sites of the whole sample. Here
536 $\{\lambda_i\}$ distribute uniformly within the interval of $[-W, W]$ with W being the disorder strength.
537 To preserve the inversion symmetry, the on-site energies of the rest sites of the sample are
538 determined by inversion. Namely, each pair of sites connected by the inversion symmetry
539 shares the same on-site energy. The calculations are performed in samples with lattice size
540 $L = 31$. Because of the random character, we average the \mathbf{r} -space Euler number over 100

541 sample configurations for every W . A higher accuracy can be achieved by adopting samples
542 with larger sizes and doing the statistical average for more samples.

543 H.3 Structural disorder

544 In order to further investigate the applicability of the real-space formula of the Euler number,
545 we study the effect of in-plane structural disorder in finite samples which lack the translational
546 periodicity and all other spatial symmetries [101–103]. To illustrate this effect, we assign
547 random atomic displacement $\delta = (d \cos \theta, d \sin \theta)$ away from its equilibrium position for each
548 atom of the aforementioned 2D perfect square lattice, as depicted in Fig. S7(a). Here, θ is a
549 random azimuth angle uniformly distributed in the interval $[0, 2\pi)$. The amplitude d of atomic
550 displacements are determined by Gaussian distributions with standard deviation $\sigma = 0.2$. For
551 the special structural disorder case but preserving the inversion symmetry, one can assign the
552 random atomic displacement only to the first half of the lattice, and determine the locations
553 of atoms in the other half of the lattice by the inversion symmetry. As the structure becomes
554 disordered, the hopping integrals in Eq. (8) also adjust according to local structural distortions.

555 H.4 Twisted boundary condition for quasicrystals

556 For an octagonal sample of the Ammann-Beenker-tiling quasicrystal, we calculate the energy
557 spectrum using both OBC and the twisted boundary condition (TBC). To apply TBC, we arti-
558 ficially glued the opposite edges of an octagonal polygon. Specifically, for an octagonal polygon
559 with the edge width of L_{edge} , we label the edges as E_p ($p = 1, 2, \dots, 8$) anticlockwise. For the
560 edge E_p , we define a translation operator, which is perpendicular to the edge and translates
561 the octagon by a distance of $2L_{edge}$. By applying the translation operator to the finite octag-
562 onal quasicrystal so that edge E_p of the sample connects with the opposite edge $E_{(p+4) \bmod 8}$
563 of the translated image sample. Then we consider the hopping cross the edge between site i
564 in the octagonal sample and site \tilde{j} in the image sample. These extra hoppings also follow the
565 Slater-Koster parameterization and have inverse-square decay with the distance (i.e., $|r_{ij}|^{-2}$).
566 Therefore, in addition to the intersite hoppings between sites inside the sample, we also con-
567 sider extra hoppings between sites near opposite edges. Importantly, by applying TBC, we not
568 only get rid of the effect of the open boundary but also restore the 8-fold symmetry of the
569 quasicrystal.

570 H.5 Construction of composite Wannier function

571 Since the real-space Euler number obtained in Eq. (6) can only be calculated in Wannier basis,
572 a crucial step in the numerical calculation is to construct the Wannier function in systems even
573 without the spatial translational symmetry.

574 One possible way to construct the real-space Wannier function is the functional optimiza-
575 tion method. The eigenfunctions ϕ_m associated with the energy index m can be obtained by
576 solving the eigenvalue problem of the Hamiltonian H . Then the required composite Wannier
577 functions W_n are constructed from ϕ_m as

$$W_n = \sum_m S_{nm} \phi_m, \quad (\text{H.3})$$

578 via the unitary transformation S that can be considered as the combination of a phase term
579 and a band matrix [93], which can be numerically obtained by minimizing the Wannier spread
580 functional

$$\Omega = \sum_n [\langle W_n | r^2 | W_n \rangle - \langle W_n | r | W_n \rangle^2]. \quad (\text{H.4})$$

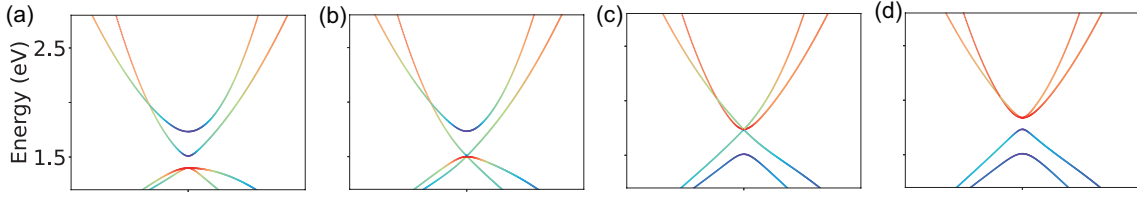


Figure S1: The evolution of band structure around the phase transition in Fig. 1(b). Orbital-resolved band structures near Γ point for the square lattice based on Eq. (8) with different on-site energy difference Δ . (a) $\Delta = 6.76$ eV (region I, $e = 1$). (b) $\Delta = \Delta_1 = 6.86$ eV (the critical point between region I and II). (c) $\Delta = \Delta_2 = 7.10$ eV (the critical point between region II and III). (d) $\Delta = 7.20$ eV (region III, $e = 0$).

581 Once the Wannier functions are constructed, the internal and coordinate spaces can be eas-
 582 ily separated and the real-space Euler number can be calculated straightforwardly using the
 583 formula given in Eq. (6).

584 In the functional optimization process, a key factor is the selection of the initialization. In
 585 our case, this is the initial value of W_n . In principle, the initial Wannier function can be set
 586 arbitrarily. However, to obtain a more efficient and convergent result, the initial function can
 587 be chosen as the Wannier function obtained in a translational invariant system. To be more
 588 specific, for disordered lattices, the Wannier function constructed through the Fourier trans-
 589 formation of the Block functions obtained in perfect lattice is a great initial function. However,
 590 it might be hard to find such a \mathbf{k} -space analog in quasicrystal and even totally amorphous sys-
 591 tems. In our work, the initial Wannier function of the quasicrystal is obtained from that of a
 592 16×73 rectangle lattice in Fig. 2.

593 As for the fully non-periodic systems where the gauge optimization fails to work, other
 594 methods such as the Iterated projected position (IPP) algorithm are supposed to be considered
 595 without the initialization requirement [104].

596 Another issue to be clarified is the ordering of occupied states within a certain cell \mathbf{r} . It can
 597 be determined by the corresponding diagonal element of the Hamiltonian on the composite
 598 Wannier basis. We also noticed that the local Euler marker is attached to only an additional
 599 minus sign when this ordering is inverted. Therefore, more conveniently, the sign of local
 600 Euler markers can be set to satisfy the continuity of these markers.

601 H.6 Numerical calculation of the \mathbf{k} -space Euler number

602 Generally speaking, non-accidental degenerate points (nodes) between the nontrivial occupied
 603 bands are common in \mathbf{k} -space [47]. To numerically calculate the \mathbf{k} -space Euler number in this
 604 context, we employ the following expression:

$$|e| = \int_{\mathcal{D}} e(\mathcal{F}) - \int_{\partial \mathcal{D}} \langle u_1 | \nabla | u_2 \rangle \cdot \frac{d\mathbf{k}}{2\pi}, \quad (\text{H.5})$$

605 where $e(\mathcal{F}) = (1/\pi) \langle \partial_{[k_x]} u_1(\mathbf{k}) | \partial_{[k_y]} u_2(\mathbf{k}) \rangle dk_x \wedge dk_y$, and \mathcal{D} represents the region in the Brill-
 606 ouin zone (BZ) containing those nodes.

607 I More numerical results

608 I.1 Band structures around the topological phase transition in Fig. 1(b)

609 Here we discuss three regions presented in Fig. 1(b) in the main text in detail. These regions
 610 are divided by two critical points $\Delta_1 = 6.86$ and $\Delta_2 = 7.10$ eV. As illustrated in Fig. S1(a), there
 611 is initially a double band inversions occurring around Γ point with $\Delta < \Delta_1$, which accounts
 612 for the nontrivial band topology with $|e| = 1$. This is consistent with the calculations of the
 613 r -space Euler number in the main text, demonstrating that the phase in region I is indeed the
 614 Euler insulator.

615 As the onsite difference Δ increases, the gap decreases gradually and eventually closes at
 616 Δ_1 , as shown in Fig. S1(b). The closing of the gap indicates a topological phase transition.
 617 However, unlike the usual situation of a single band inversion where the gap reopens immedi-
 618 ately after closure accompanied by a sharp change in the topological invariant, our model has
 619 an intermediate gapless region before the gap reopens at Δ_2 as shown in Fig. S1(c). From the
 620 perspective of the band topology, region II is a one-band-inverted phase without protection
 621 from the Euler topology, which accounts for the continuous decreasing of the r -space Euler
 622 number in region II [see Fig. 1(b) in the main text]. In addition, the distinction between the
 623 k -space and r -space Euler number in region II is also due to the closed gap that brings up
 624 the discrimination between \hat{P} projected and the well-defined occupied states. When $\Delta > \Delta_2$
 625 as shown in Fig. S1(d), the gap reopens and there is no band inversion at Γ point anymore.
 626 This phase can be adiabatically connected to the atomic limit without gap closure. Therefore,
 627 region III is a trivial insulator with $e = 0$ as expected.

628 I.2 Convergence of the real-space Euler number with decreasing band gap

629 There is a numerical deviation of both k -space and r -space Euler number from an exact inte-
 630 ger in regions I and III near the critical points in Fig. 1(b). Here we examine the numerical
 631 deviation in region I. As presented in the main text, the r -space Euler number equals the exact
 632 one within a correction of order $\mathcal{O}(1/(L\Delta E))$ for systems with lattice size L and energy gap
 633 ΔE . For a system with fixed lattice size L , the numerical correction is inversely proportional to
 634 the band gap: $1 - |e| \propto 1/\Delta E$, where e is the r -space Euler number. To examine the conver-
 635 gence of our r -space formulation as a function of on-site energy difference Δ , we calculate the
 636 band gap ΔE and the r -space Euler number in region I for a sample with fixed L . As shown
 637 in Fig. S2, we plot the Δ dependence of both ΔE and $a_E/1 - |e|$, where $a_E = 3.125$ meV is a
 638 fitting parameter. The inverse of the numerical correction fits well with ΔE as expected, in-
 639 dicating that the numerical correction becomes significant near the critical point of the phase
 640 transition. Nevertheless, such numerical correction can be diminished by increasing the lattice
 641 size.

642 I.3 Convergence of the real-space Euler number with increasing lattice size

643 To examine the convergence of real-space Euler number as a function of lattice size L , we
 644 further calculate larger systems with the size L up to 90. We consider the pristine lattice with
 645 PBC or OBC and a disordered lattice with $W = 1.0$ eV. For the disordered case, we perform
 646 an average of the r -space Euler number over 10 samples for each L . As shown in Fig. S3, the
 647 curve of the disordered case has not saturated yet but converges slowly towards the quantized
 648 value of 1. To further check the convergent behavior, we perform a fitting (see the fitting line
 649 in Fig. S3) to estimate the lattice size for the real-space Euler number to reach the quantized
 650 value with the error less than 1%. It is found that the required lattice sizes are $L \approx 355$ for
 651 the pristine OBC case and $L \approx 570$ for the disordered case respectively, which are beyond the

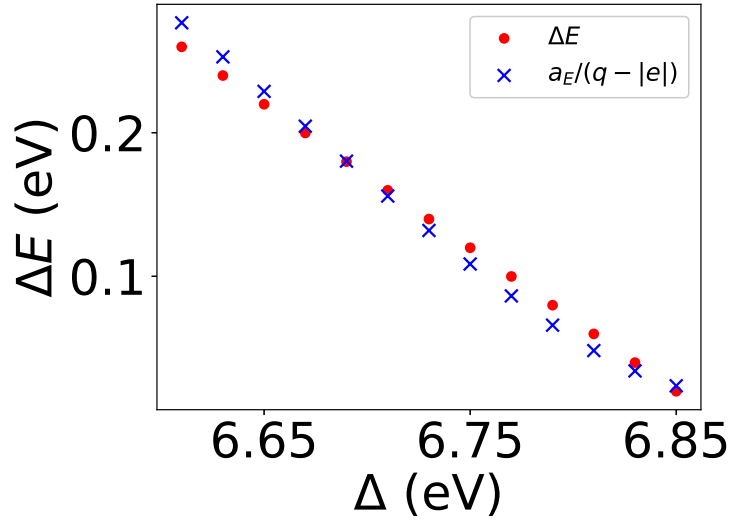


Figure S2: The on-site energy difference Δ dependence of ΔE and $q - |e|$ with $a_E = 3.125$ meV. Here q denotes the expected quantized value and is equal to 1 in this case.

652 memory limit of our computational resource. As a comparison, the same estimation for the
 653 pristine PBC case without disorder shows that a much smaller lattice size of $L \approx 63$ is required
 654 to reach the same accuracy. This is because the energy gap is $\Delta E = 0.469$ eV in the pristine
 655 PBC case, but for the disordered case with $W = 1.0$ eV, the corresponding averaged gap reduces
 656 significantly to $\Delta E = 0.0583$ eV, which is one order of magnitude smaller than the former. This
 657 dependence is illustrated in Fig. S4. As the numeric correction is on the order of $\mathcal{O}(1/(L\Delta E))$
 658 for systems with lattice size L and energy gap ΔE , the much slower convergence rate of the
 659 disordered case is mainly due to the significant reduction of the energy gap reduction in the
 660 presence of disorder.

661 I.4 Deviation of real-space Euler number with OBC

662 In this section, we discuss the deviation of r -space Euler number with OBC. The OBC case
 663 shows a similar linear dependence between $1/L$ and the numerical deviation $\Delta e = 1 - |e|$ with
 664 slower convergent behavior. This means that the OBC includes an additional effect which is
 665 up to order $\mathcal{O}(1/L)$ as well. Notice that the Euler number is obtained by averaging the local
 666 Euler markers at all sites. Since the sites far from boundaries are supposed to preserve similar
 667 properties to those in periodic systems, such deviation originates from the sites close to the
 668 boundary, which contributes $\mathcal{O}(L_{edge}/A) = \mathcal{O}((L^2 - (L-2)^2)/L^2) = \mathcal{O}(4L/L^2) = \mathcal{O}(4/L)$ as
 669 expected. Here L_{edge} and A are the number of sites in the boundary and the whole sample,
 670 respectively. This additional factor accounts for the slope approximated to $1/4$ in Fig. S5,
 671 confirming the effect on r -space Euler number from the edge.

672 I.5 Local Euler markers in lattices with on-site disorder in Fig. 1(c)

673 In Fig. 1(c) in the main text, we illustrate another intriguing type of topological phase transi-
 674 tion induced by on-site disorder. The averaged r -space Euler number e decreases from 1 to 0
 675 with increasing the disorder strength W . Here we present the spatial distribution of the local
 676 Euler marker of the sample with PBC at different disorder strengths W , as shown in Fig. S6. At
 677 a relatively weak disorder of $W = 1.2$ eV, the system maintains its nontrivial Euler characteris-
 678 tics. Predominantly, the grid points exhibit nontrivial local Euler markers $e(\mathbf{r}) \approx 1$ with a few

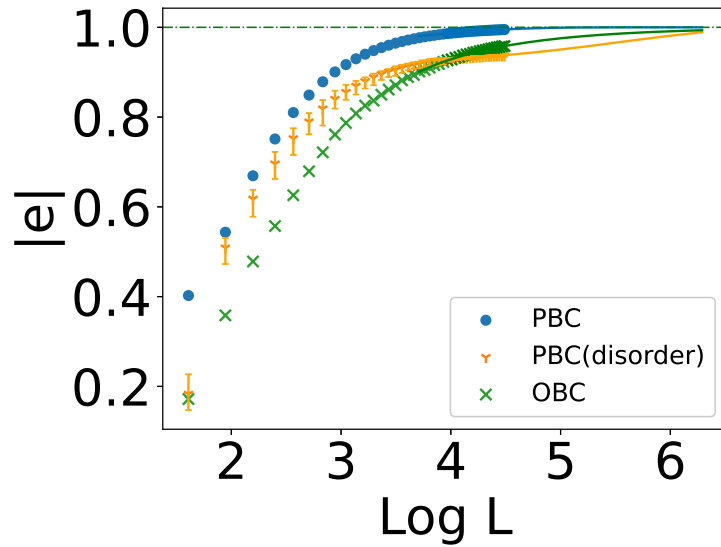


Figure S3: The lattice size L dependence of the r -space Euler number calculated without and with on-site energy disorder ($W = 1.0$ eV) using PBC, and without disorder using OBC. Fitting curves are added for each case.

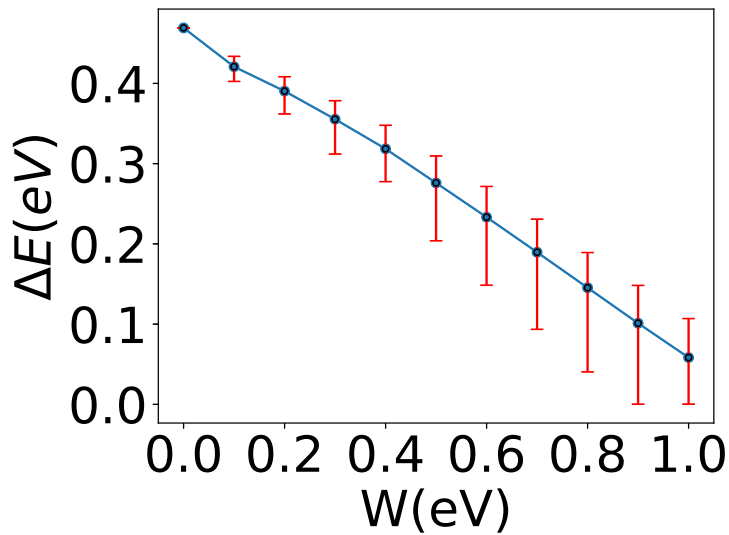


Figure S4: The energy gap ΔE versus on-site energy disorder strength W . For each W , the configuration average is performed over 100 realizations of 51×51 disordered lattices with PBC.

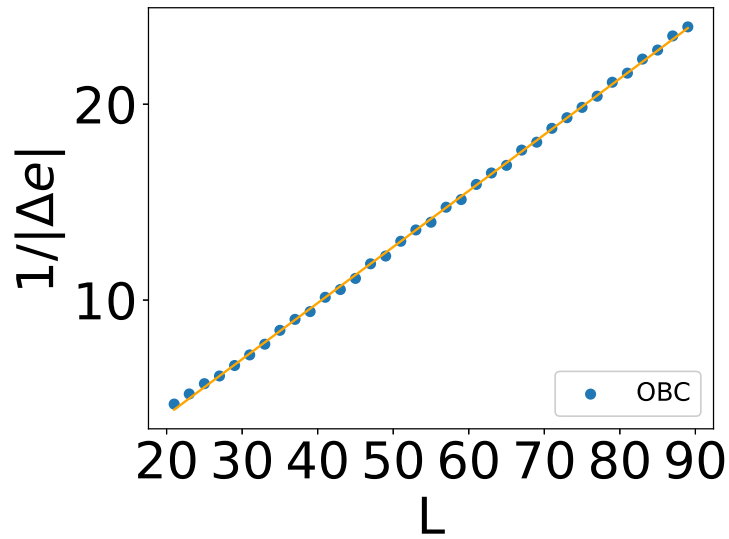


Figure S5: The inverse of the deviation of the r -space Euler number Δe versus lattice size L with OBC.

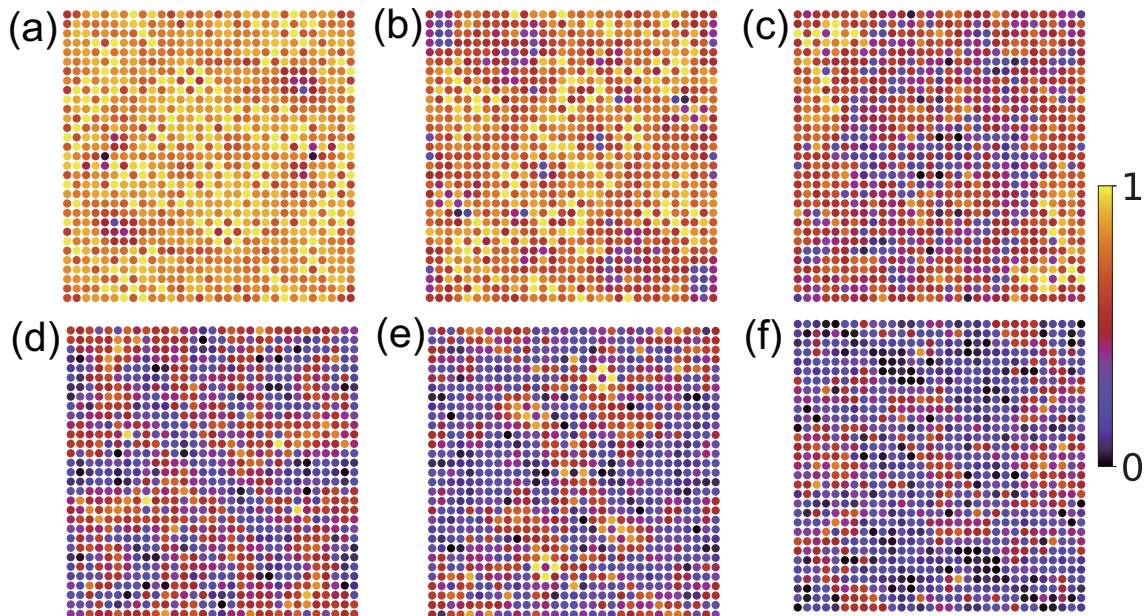


Figure S6: The real-space distribution of local Euler markers $e(\tau)$ in 31×31 square lattices with PBC at different disorder strength W . (a) $W = 1.2$ eV. (b) $W = 1.4$ eV. (c) $W = 1.6$ eV. (d) $W = 1.8$ eV. (e) $W = 2.0$ eV. (f) $W = 2.2$ eV.

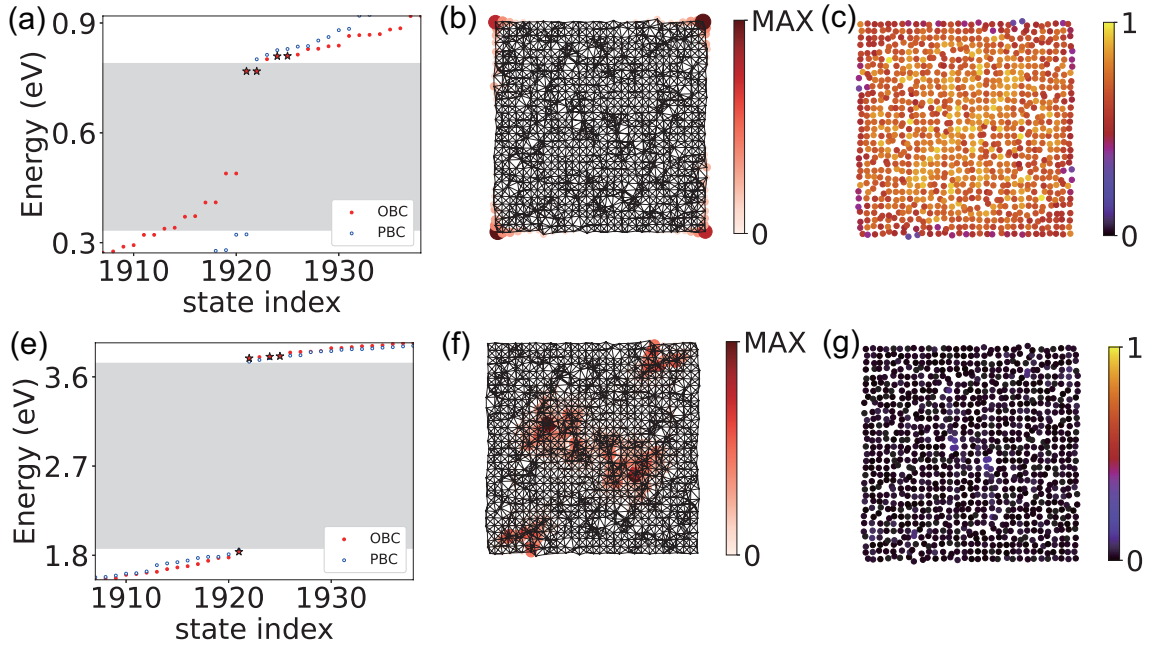


Figure S7: The disordered square lattice model that exhibits band inversions between the (p_x, p_y) and $(d_{x^2-y^2}, d_{xy})$ orbitals. The relevant parameters are as follows: $L = 31$, $\epsilon_{p_x, p_y} = 1.58$, $\epsilon_{d_{x^2-y^2}, d_{xy}} = -0.42$, $V_{pp\sigma} = -0.565$, $V_{pp\pi} = -0.044$, $V_{pd\sigma} = 0.773$, $V_{pd\pi} = 0.335$, $V_{dd\sigma} = 0.444$, $V_{dd\pi} = 0.224$, $V_{dd\delta} = 0.659$ eV. (a) The energy eigenvalues versus the state index in the vicinity of the Fermi level for the disordered square lattice with PBC and OBC. (b) The spatial distribution of the corner states [red stars in (a)]. (c) The real-space distribution of the local Euler marker $e(\mathbf{r})$ for the disordered system with OBC. (e-g) Corresponding results as (a-c) for a trivial state with $e = 0$ (The onsite energy difference is set to $\Delta = 6$ eV).

679 isolated points having vanished $e(\mathbf{r}) \approx 0$, as shown in Fig. S6(a). However, by increasing the
 680 disorder strength W , a noteworthy transformation occurs: the number of trivial points with
 681 $e(\mathbf{r}) \approx 0$ increases, and the trivial area enlarges in size, eventually leaving the nontrivial area
 682 shrinks to an isolated region in the sample [see Fig. S6(c)]. This isolated nontrivial region
 683 with $e(\mathbf{r}) \approx 1$ diminishes in size gradually as W continues to increase, ultimately fragmenting
 684 into small segments [see Fig. S6(d,e)]. Upon reaching $W \geq 2.2$ eV, the situation undergoes a
 685 significant shift. As shown in Fig. S6(f), none of the grid points exhibits nontrivial local Euler
 686 markers, indicating that the system is driven into a trivial phase by strong on-site disorder.
 687 Notably, this type of topological phase transition differs from those in disordered Chern insu-
 688 lators and quantum spin Hall insulators, where a sudden jump of topological invariants occurs
 689 at the critical point [25]. Instead, the disorder-induced transition in this model manifests as
 690 a more continuous evolution. Physically, we conjecture this to be due to the disorder-induced
 691 renormalization of the parameter Δ which dominates the transition from the Euler insulator
 692 to the trivial phase through the intermediate gapless phase, as depicted in Fig. 1(b).

693 I.6 Euler insulator in lattice with moderate structural disorder

694 In this section, we study the Euler topology of a square lattice with moderate structural dis-
 695 order. We specifically preserve the inversion symmetry at this stage, for comparison with
 696 the case breaking all spatial symmetries presented in Fig. 3 of the main text. To construct
 697 the structurally disordered square lattice [34, 35, 79, 101–103], we add random displacement
 698 $\tilde{\delta} = d(\cos \theta, \sin \theta)$ away from its equilibrium position for each site in one-half sample ($\tau_{1/2}$)

699 of the square lattice, and assign the displacements for the other half to preserve inversion
700 symmetry. Here θ and d are determined by uniform distributions in the interval $[0, \pi)$ and
701 Gaussian distributions with standard deviation $\sigma = 0.2$, respectively. As shown in Fig. S7(a),
702 the energy spectrum of the structurally disordered lattice with OBC exhibits 4 states at the
703 Fermi level in the bulk gap obtained using PBC (grey area). We plot the spatial distribution of
704 these states and find that they are well localized at 4 corners of the sample [see Fig. S7(b)],
705 implying its higher-order topological feature. Because of the effect of the structural disorder,
706 the corner states move upwards to the bottom of the unoccupied bulk states. Furthermore, we
707 analyze the distribution of the local Euler marker in the finite sample with structural disorder,
708 as shown in Fig. S7(c). The plot confirms that the local Euler markers $e(\mathbf{r})$ are close to the
709 expected value of 1 in the bulk of the sample, while they deviate in the boundary region. As
710 expected, the sum of $e(\mathbf{r})$ over the whole finite sample does not vanish but yields the desired
711 Euler number which should converge to the quantized value with increasing lattice size. Con-
712 sequently, we can obtain an accurate \mathbf{r} -space Euler number by averaging $e(\mathbf{r})$ over an internal
713 region of the sample to get rid of the boundary deviation. As a comparison, we also perform
714 a similar calculation for a trivial phase (see the bottom panels in Fig. S7). As illustrated in
715 Fig. S7(g), the local Euler marker is almost 0 all over the sample, unambiguously indicating
716 the trivial nature of the state.

717 I.7 The upward shift of eigenenergies of corner states with decreasing bulk gap

718 In this section, we discuss the upward shift of eigenenergies of corner states with increasing
719 on-site energy. As illustrated in Fig. 3 and Fig. S7, introducing structural disorder leads to
720 the upward shift of the eigenenergies of corner states. In fact, this effect originates from the
721 decreasing energy gap. In structurally disordered samples, the decrease is attributed to the
722 increasing disorder amplitude. Additionally, the adjustment of the on-site energy can also
723 lead to a smaller bulk gap. As discussed in appendix I.1, in region I, we can lift the on-site
724 energy of p -orbitals such that the bulk gap will decrease and finally vanish at critical point Δ_1 .
725 Therefore, for comparison purposes, we consider a square model with the same parameters as
726 in Fig. 3 except for the on-site energy difference. As illustrated in Fig. S8(a), increasing the
727 on-site energy difference shows a similar upward shift effect to that observed in structurally
728 disordered lattices. These shifting states near the upper bound of the PBC gap are spatially
729 localized at four corners, as shown in Fig. S8(b). These results show the similarity between
730 the effect of on-site energy difference and structural disorder on the upward shifting, which
731 can be explained as the effect of the decreasing bulk gap.

732 I.8 Validation in other models with different Euler numbers

733 In the main text, we present the results based on the tight-binding model with the Euler num-
734 ber $e = 1$. Now we show that our proposed \mathbf{r} -space formula of the Euler number also applies
735 to other models with different Euler numbers as well. Different from the tight-binding Hamil-
736 tonian in Eq. (8) based on the atomic orbital basis, we consider a generic \mathcal{PT} -symmetric
737 four-band Bloch Hamiltonian $H^{(\chi_1, \chi_2)}(\mathbf{k})$ with (χ_1, χ_2) representing the Euler number of the
738 upper and lower two-band subspace respectively [99].

739 Specifically, we take $(\chi_1, \chi_2) = (2, 2)$ as an example. The time-reversal \hat{T} and inversion \hat{P}
740 operators can be expressed as

$$\begin{aligned}\hat{T} &= -i\Gamma_{22}\hat{K}, \\ \hat{P} &= i\Gamma_{22},\end{aligned}\tag{I.1}$$

741 where $\Gamma_{i,j} = \sigma_i \otimes \sigma_j$ are 4×4 Dirac matrices and \hat{K} is the complex conjugation. The minimal

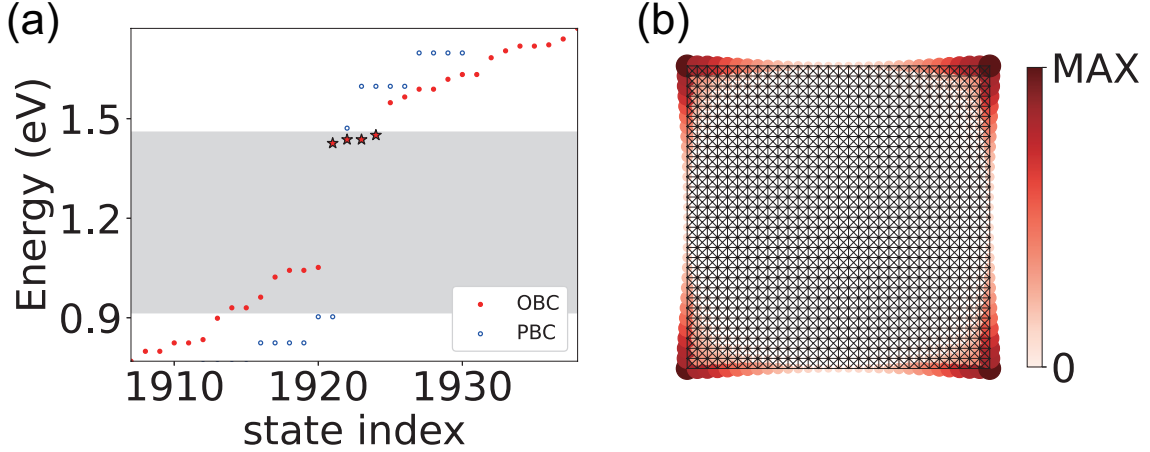


Figure S8: The square lattice model that exhibits band inversions between the (p_x, p_y) and $(d_{x^2-y^2}, d_{xy})$ orbitals. The relevant parameters are as follows: $L = 31$, $\epsilon_{p_x, p_y} = 2.73$, $\epsilon_{d_{x^2-y^2}, d_{xy}} = -0.42$, $V_{pp\sigma} = -0.565$, $V_{pp\pi} = -0.044$, $V_{pd\sigma} = 0.773$, $V_{pd\pi} = 0.335$, $V_{dd\sigma} = 0.444$, $V_{dd\pi} = 0.224$, and $V_{dd\delta} = 0.659$ eV. (a) Energy spectrum of the square lattice with PBC and OBC. Four corner states in the gap are highlighted by red stars. (b) Spatial distribution of the corner states [red stars in (a)].

742 four-band Hamiltonian $H^{(2,2)}(\mathbf{k})$ can be expressed as

$$H^{(2,2)}(\mathbf{k}) = \sin k_1 \Gamma_{01} + \sin k_2 \Gamma_{03} - \left[\frac{1}{2} + \frac{1}{2}(\cos k_1 + \cos k_2) + \frac{3}{2} \cos(k_1 + k_2) \Gamma_{22} + \frac{1}{2} \Gamma_{13} \right]. \quad (\text{I.2})$$

743 To calculate the \mathbf{r} -space Euler number in a finite $L \times L$ supercell of the square lattice, we
 744 construct the real-space Hamiltonian $H^{(2,2)}$ by performing the Fourier transformation to the
 745 Bloch Hamiltonian $H^{\chi_1, \chi_2}(\mathbf{k})$, which yields

$$H^{\chi_1, \chi_2} = \sum_{ij} \sum_{\mu\nu} \sum_{\mathbf{k} \in \text{BZ}} e^{i\mathbf{k} \cdot (\mathbf{r}_i - \mathbf{r}_j)} [H^{\chi_1, \chi_2}(\mathbf{k})]_{\mu\nu} c_{i\mu}^\dagger c_{j\nu}. \quad (\text{I.3})$$

746 Here, \mathbf{r}_i is the lattice vector of the i -th site in the square lattice, and $c_{i\mu}^\dagger$ ($c_{i\mu}$) is electron creation
 747 (annihilation) operator on the μ orbital at the i -th site. For simplicity, we only consider nearest-
 748 neighbor pairs $\langle ij \rangle$ in the lattice. The hopping between site i and j is determined by the
 749 summation over \mathbf{k} in the BZ, $t_{\mu\nu}(\mathbf{r}_{ij}) = \sum_{\mathbf{k} \in \text{BZ}} e^{i\mathbf{k} \cdot (\mathbf{r}_i - \mathbf{r}_j)} [H^{\chi_1, \chi_2}(\mathbf{k})]_{\mu\nu}$. The on-site energies
 750 are given by $\epsilon_\mu = t_{\mu\mu}(\mathbf{0})$.

751 The calculated results are shown in Fig. S9. Similar to the Euler insulator with $e = 1$
 752 presented in the main text, the OBC energy spectrum exhibits some states in the bulk gap.
 753 However, these in-gap states are localized on edges instead of corners of the finite sample [see
 754 Fig. S9(c)]. This indicates distinct topological behaviors from the topological Euler insulator
 755 with $e = 1$. According to the relation between the second Stiefel-Whitney number and the
 756 Euler number $w_2 = e \pmod{2}$, the Euler insulator with $e = 1$ is also a Stiefel-Whitney insulator
 757 with $w_2 = 1$ which exhibits higher-order topology with corner states in the presence of ad-
 758 ditional chiral symmetry [49, 105]. In contrast, the Euler phase with $e = 2$ leads to a trivial
 759 second Stiefel-Whitney number $w_2 = 0$. Nevertheless, the system associated with the nonzero
 760 Euler number still has a fragile band topology [50]. As shown in Fig. S9 (d), we plot the real-
 761 space distribution of the local Euler marker, which exhibits similar bulk domination and edge
 762 diminution behavior as those studied in the main text. Remarkably, the local Euler markers

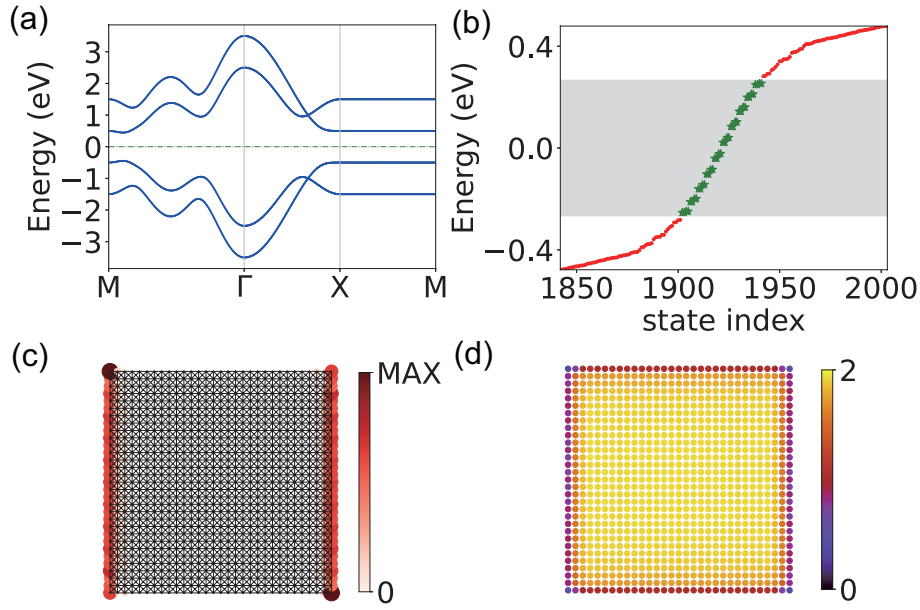


Figure S9: The topological Euler phase with $(\chi_1, \chi_2) = (2, 2)$ in a square lattice based on the minimal four-band model in Eq. (I.3). (a) Band structures of the four-band model in the square lattice. (b) Energy spectrum of a finite sample with OBC. The lattice size is $L = 31$. The bulk gap obtained using PBC is marked in grey. (c) Real-space distribution of the in-gap states [highlighted by green stars in (b)] which are localized on two opposite edges of the finite sample. (d) The real-space distribution of the local Euler marker $e(\mathbf{r})$ in the sample with OBC.

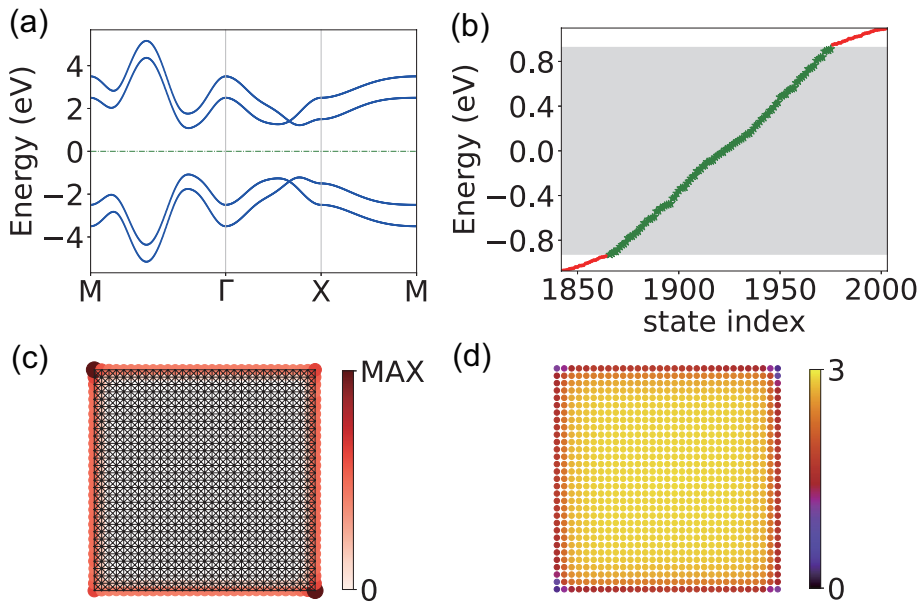


Figure S10: The topological Euler phase with $(\chi_1, \chi_2) = (3, 1)$ in a square lattice based on the minimal four-band model. (a) Band structures of the four-band model in the square lattice. (b) Energy spectrum of a finite sample with OBC. The lattice size is $L = 31$. The bulk gap obtained using PBC is marked in grey. (c) Real-space distribution of the in-gap states [highlighted by green stars in (b)] which are localized on the edges of the finite sample. (d) The real-space distribution of the local Euler marker $e(\mathbf{r})$ in the sample with OBC.

763 inside the bulk are close to the expected value of 2, which results in the averaged r -space
764 Euler number being $e = 2$.

765 We further validate our r -space Euler number in another four-band model with different
766 Euler numbers for occupied and unoccupied bands. Specifically, we chose the minimal model
767 with $(\chi_1, \chi_2) = (3, 1)$, which can be formulated as

$$H^{(3,1)}(\mathbf{k}) = \begin{pmatrix} \bar{a} \\ \bar{b} \\ \bar{c} \end{pmatrix}^T \cdot \Gamma \cdot \begin{pmatrix} \bar{a} \\ \bar{b} \\ \bar{c}' \end{pmatrix}, \quad (\text{I.4})$$

768 with

$$\Gamma = \begin{pmatrix} -\Gamma_{33} & -\Gamma_{13} & \Gamma_{01} \\ \Gamma_{31} & \Gamma_{11} & \Gamma_{03} \\ \Gamma_{10} & -\Gamma_{30} & -\Gamma_{22} \end{pmatrix} \quad (\text{I.5})$$

769 and

$$\begin{aligned} \bar{a} &= \sin k_1, \\ \bar{b} &= \sin k_2 \\ \bar{c} &= \frac{1}{2}(1 + (\cos k_1 + \cos k_2) + 3\cos(k_1 + k_2)), \\ \bar{c}' &= \frac{1}{2}(3 - 2(\cos k_1 + \cos k_2) - \cos(k_1 + k_2)). \end{aligned} \quad (\text{I.6})$$

770 The results of the minimal model with $(\chi_1, \chi_2) = (3, 1)$ are illustrated in Fig. S10. In this
771 case, the unbalanced $|\chi_1| \neq |\chi_2|$ leads to the lack of additional symmetry of the system [106].
772 Consequently, although the system is a topological phase with nontrivial Stiefel-Whitney num-
773 ber $w_2 = 1$ because of the odd Euler number of the occupied bands, there is no additional
774 symmetry to ensure the localization at the corner. Therefore, this phase does not exhibit the
775 higher-order corner characteristics of conventional Stiefel-Whitney insulators [107–111].

776 References

- 777 [1] K. v. Klitzing, G. Dorda and M. Pepper, *New method for high-accuracy determination of*
778 *the fine-structure constant based on quantized Hall resistance*, Phys. Rev. Lett. **45**, 494
779 (1980), doi:[10.1103/PhysRevLett.45.494](https://doi.org/10.1103/PhysRevLett.45.494).
- 780 [2] D. J. Thouless, M. Kohmoto, M. P. Nightingale and M. den Nijs, *Quantized Hall con-*
781 *ductance in a two-dimensional periodic potential*, Phys. Rev. Lett. **49**, 405 (1982),
782 doi:[10.1103/PhysRevLett.49.405](https://doi.org/10.1103/PhysRevLett.49.405).
- 783 [3] M. Kohmoto, *Topological invariant and the quantization of the Hall conductance*, Annals
784 of Physics **160**(2), 343 (1985), doi:[https://doi.org/10.1016/0003-4916\(85\)90148-4](https://doi.org/10.1016/0003-4916(85)90148-4).
- 785 [4] B. I. Halperin, *Quantized Hall conductance, current-carrying edge states, and the exis-*
786 *tence of extended states in a two-dimensional disordered potential*, Phys. Rev. B **25**, 2185
787 (1982), doi:[10.1103/PhysRevB.25.2185](https://doi.org/10.1103/PhysRevB.25.2185).
- 788 [5] Y. Hatsugai, *Chern number and edge states in the integer quantum Hall effect*, Phys. Rev.
789 Lett. **71**, 3697 (1993), doi:[10.1103/PhysRevLett.71.3697](https://doi.org/10.1103/PhysRevLett.71.3697).

- 790 [6] D. Xiao, M.-C. Chang and Q. Niu, *Berry phase effects on electronic properties*, Rev. Mod.
791 Phys. **82**, 1959 (2010), doi:[10.1103/RevModPhys.82.1959](https://doi.org/10.1103/RevModPhys.82.1959).
- 792 [7] M. Z. Hasan and C. L. Kane, *Colloquium: Topological insulators*, Rev. Mod. Phys. **82**,
793 3045 (2010), doi:[10.1103/RevModPhys.82.3045](https://doi.org/10.1103/RevModPhys.82.3045).
- 794 [8] X.-L. Qi and S.-C. Zhang, *Topological insulators and superconductors*, Rev. Mod. Phys.
795 **83**, 1057 (2011), doi:[10.1103/RevModPhys.83.1057](https://doi.org/10.1103/RevModPhys.83.1057).
- 796 [9] T. Fukui, Y. Hatsugai and H. Suzuki, *Chern numbers in discretized Brillouin zone: Efficient
797 method of computing (spin) Hall conductances*, J. Phys. Soc. Japan **74**(6), 1674 (2005),
798 doi:[10.1143/JPSJ.74.1674](https://doi.org/10.1143/JPSJ.74.1674).
- 799 [10] A. Kitaev, *Anyons in an exactly solved model and beyond*, Annals of Physics **321**(1), 2
800 (2006), doi:<https://doi.org/10.1016/j.aop.2005.10.005>.
- 801 [11] R. Bianco and R. Resta, *Mapping topological order in coordinate space*, Phys. Rev. B **84**,
802 241106 (2011), doi:[10.1103/PhysRevB.84.241106](https://doi.org/10.1103/PhysRevB.84.241106).
- 803 [12] E. Prodan, *Non-commutative tools for topological insulators*, New Journal of Physics
804 **12**(6), 065003 (2010), doi:[10.1088/1367-2630/12/6/065003](https://doi.org/10.1088/1367-2630/12/6/065003).
- 805 [13] T. A. Loring and M. B. Hastings, *Disordered topological insulators via C^* -algebras*, Euro-
806 physics Letters **92**(6), 67004 (2011), doi:[10.1209/0295-5075/92/67004](https://doi.org/10.1209/0295-5075/92/67004).
- 807 [14] D. Toniolo, *On the Bott index of unitary matrices on a finite torus*, Lett. Math. Phys.
808 **112**(6), 126 (2022), doi:[10.1007/s11005-022-01602-6](https://doi.org/10.1007/s11005-022-01602-6).
- 809 [15] M. B. Hastings and T. A. Loring, *Topological insulators and C^* -algebras:
810 Theory and numerical practice*, Annals of Physics **326**(7), 1699 (2011),
811 doi:<https://doi.org/10.1016/j.aop.2010.12.013>.
- 812 [16] T. A. Loring, *K -theory and pseudospectra for topological insulators*, Annals of Physics
813 **356**, 383 (2015), doi:<https://doi.org/10.1016/j.aop.2015.02.031>.
- 814 [17] E. Prodan, *Disordered topological insulators: a non-commutative geometry perspec-
815 tive*, Journal of Physics A: Mathematical and Theoretical **44**(11), 113001 (2011),
816 doi:[10.1088/1751-8113/44/11/113001](https://doi.org/10.1088/1751-8113/44/11/113001).
- 817 [18] M. D. Caio, G. Möller, N. R. Cooper and M. J. Bhaseen, *Topological marker currents in
818 Chern insulators*, Nature Physics **15**(3), 257 (2019), doi:[10.1038/s41567-018-0390-7](https://doi.org/10.1038/s41567-018-0390-7).
- 819 [19] E. Prodan, T. L. Hughes and B. A. Bernevig, *Entanglement spectrum of a
820 disordered topological Chern insulator*, Phys. Rev. Lett. **105**, 115501 (2010),
821 doi:[10.1103/PhysRevLett.105.115501](https://doi.org/10.1103/PhysRevLett.105.115501).
- 822 [20] I. C. Fulga, D. I. Pikulin and T. A. Loring, *Aperiodic weak topological superconductors*,
823 Phys. Rev. Lett. **116**, 257002 (2016), doi:[10.1103/PhysRevLett.116.257002](https://doi.org/10.1103/PhysRevLett.116.257002).
- 824 [21] I. Mondragon-Shem, T. L. Hughes, J. Song and E. Prodan, *Topological criticality in
825 the chiral-symmetric AIII class at strong disorder*, Phys. Rev. Lett. **113**, 046802 (2014),
826 doi:[10.1103/PhysRevLett.113.046802](https://doi.org/10.1103/PhysRevLett.113.046802).
- 827 [22] S. Velury, B. Bradlyn and T. L. Hughes, *Topological crystalline phases in
828 a disordered inversion-symmetric chain*, Phys. Rev. B **103**, 024205 (2021),
829 doi:[10.1103/PhysRevB.103.024205](https://doi.org/10.1103/PhysRevB.103.024205).

- 830 [23] J. Claes and T. L. Hughes, *Disorder driven phase transitions in weak AIII topological*
831 *insulators*, Phys. Rev. B **101**, 224201 (2020), doi:[10.1103/PhysRevB.101.224201](https://doi.org/10.1103/PhysRevB.101.224201).
- 832 [24] H. Huang and F. Liu, *Quantum spin Hall effect and spin Bott index in a quasicrystal lattice*,
833 Phys. Rev. Lett. **121**, 126401 (2018), doi:[10.1103/PhysRevLett.121.126401](https://doi.org/10.1103/PhysRevLett.121.126401).
- 834 [25] H. Huang and F. Liu, *Theory of spin Bott index for quantum spin Hall states in nonperiodic*
835 *systems*, Phys. Rev. B **98**, 125130 (2018), doi:[10.1103/PhysRevB.98.125130](https://doi.org/10.1103/PhysRevB.98.125130).
- 836 [26] H. Huang, Y.-S. Wu and F. Liu, *Aperiodic topological crystalline insulators*, Phys. Rev. B
837 **101**, 041103 (2020), doi:[10.1103/PhysRevB.101.041103](https://doi.org/10.1103/PhysRevB.101.041103).
- 838 [27] H. Huang and F. Liu, *Comparison of quantum spin Hall states in quasicrystals and crystals*,
839 Phys. Rev. B **100**, 085119 (2019), doi:[10.1103/PhysRevB.100.085119](https://doi.org/10.1103/PhysRevB.100.085119).
- 840 [28] A. Agarwala and V. B. Shenoy, *Topological insulators in amorphous systems*, Phys. Rev.
841 Lett. **118**, 236402 (2017), doi:[10.1103/PhysRevLett.118.236402](https://doi.org/10.1103/PhysRevLett.118.236402).
- 842 [29] S. Kim, A. Agarwala and D. Chowdhury, *Fractionalization and topol-*
843 *ogy in amorphous electronic solids*, Phys. Rev. Lett. **130**, 026202 (2023),
844 doi:[10.1103/PhysRevLett.130.026202](https://doi.org/10.1103/PhysRevLett.130.026202).
- 845 [30] X. S. Wang, A. Brataas and R. E. Troncoso, *Bosonic Bott index and disorder-*
846 *induced topological transitions of magnons*, Phys. Rev. Lett. **125**, 217202 (2020),
847 doi:[10.1103/PhysRevLett.125.217202](https://doi.org/10.1103/PhysRevLett.125.217202).
- 848 [31] P. Titum, N. H. Lindner, M. C. Rechtsman and G. Refael, *Disorder-*
849 *induced Floquet topological insulators*, Phys. Rev. Lett. **114**, 056801 (2015),
850 doi:[10.1103/PhysRevLett.114.056801](https://doi.org/10.1103/PhysRevLett.114.056801).
- 851 [32] D. Toniolo, *Time-dependent topological systems: A study of the Bott index*, Phys. Rev. B
852 **98**, 235425 (2018), doi:[10.1103/PhysRevB.98.235425](https://doi.org/10.1103/PhysRevB.98.235425).
- 853 [33] B. Kang, W. Lee and G. Y. Cho, *Many-body invariants for Chern and chiral hinge insula-*
854 *tors*, Phys. Rev. Lett. **126**, 016402 (2021), doi:[10.1103/PhysRevLett.126.016402](https://doi.org/10.1103/PhysRevLett.126.016402).
- 855 [34] Y.-B. Yang, T. Qin, D.-L. Deng, L.-M. Duan and Y. Xu, *Topological amorphous metals*,
856 Phys. Rev. Lett. **123**, 076401 (2019), doi:[10.1103/PhysRevLett.123.076401](https://doi.org/10.1103/PhysRevLett.123.076401).
- 857 [35] J. D. Hannukainen, M. F. Martínez, J. H. Bardarson and T. K. Kivornig, *Local topological*
858 *markers in odd spatial dimensions and their application to amorphous topological matter*,
859 Phys. Rev. Lett. **129**, 277601 (2022), doi:[10.1103/PhysRevLett.129.277601](https://doi.org/10.1103/PhysRevLett.129.277601).
- 860 [36] W. Chen, *Universal topological marker*, Phys. Rev. B **107**, 045111 (2023),
861 doi:[10.1103/PhysRevB.107.045111](https://doi.org/10.1103/PhysRevB.107.045111).
- 862 [37] J. Sykes and R. Barnett, *Local topological markers in odd dimensions*, Phys. Rev. B **103**,
863 155134 (2021), doi:[10.1103/PhysRevB.103.155134](https://doi.org/10.1103/PhysRevB.103.155134).
- 864 [38] A. A. Markov and A. N. Rubtsov, *Local marker for interacting topological insulators*, Phys.
865 Rev. B **104**, L081105 (2021), doi:[10.1103/PhysRevB.104.L081105](https://doi.org/10.1103/PhysRevB.104.L081105).
- 866 [39] B. Irsigler, J.-H. Zheng and W. Hofstetter, *Microscopic characteristics and tomog-*
867 *raphy scheme of the local Chern marker*, Phys. Rev. A **100**, 023610 (2019),
868 doi:[10.1103/PhysRevA.100.023610](https://doi.org/10.1103/PhysRevA.100.023610).

- 869 [40] I. Mondragon-Shem and T. L. Hughes, *Robust topological invariants of topological crys-*
870 *talline phases in the presence of impurities* (2019), [1906.11847](https://doi.org/10.1103/PhysRevLett.130.186702).
- 871 [41] A. G. Grushin and C. Repellin, *Amorphous and polycrystalline routes toward a chiral spin*
872 *liquid*, Phys. Rev. Lett. **130**, 186702 (2023), doi:[10.1103/PhysRevLett.130.186702](https://doi.org/10.1103/PhysRevLett.130.186702).
- 873 [42] Y. X. Zhao, A. P. Schnyder and Z. D. Wang, *Unified theory of PT and CP invariant*
874 *topological metals and nodal superconductors*, Phys. Rev. Lett. **116**, 156402 (2016),
875 doi:[10.1103/PhysRevLett.116.156402](https://doi.org/10.1103/PhysRevLett.116.156402).
- 876 [43] Y. X. Zhao and Y. Lu, *PT -symmetric real Dirac Fermions and semimetals*, Phys. Rev. Lett.
877 **118**, 056401 (2017), doi:[10.1103/PhysRevLett.118.056401](https://doi.org/10.1103/PhysRevLett.118.056401).
- 878 [44] J. Ahn and B.-J. Yang, *Unconventional topological phase transition in two-dimensional*
879 *systems with space-time inversion symmetry*, Phys. Rev. Lett. **118**, 156401 (2017),
880 doi:[10.1103/PhysRevLett.118.156401](https://doi.org/10.1103/PhysRevLett.118.156401).
- 881 [45] J. Ahn, D. Kim, Y. Kim and B.-J. Yang, *Band topology and linking structure of nodal*
882 *line semimetals with Z_2 monopole charges*, Phys. Rev. Lett. **121**, 106403 (2018),
883 doi:[10.1103/PhysRevLett.121.106403](https://doi.org/10.1103/PhysRevLett.121.106403).
- 884 [46] Q. Wu, A. A. Soluyanov and T. Bzdušek, *Non-Abelian band topology in noninteracting*
885 *metals*, Science **365**(6459), 1273 (2019), doi:[10.1126/science.aau8740](https://doi.org/10.1126/science.aau8740).
- 886 [47] A. Bouhon, Q. Wu, R.-J. Slager, H. Weng, O. V. Yazyev and T. Bzdušek, *Non-Abelian*
887 *reciprocal braiding of Weyl points and its manifestation in ZrTe*, Nat. Phys. **16**(11), 1137
888 (2020), doi:[10.1038/s41567-020-0967-9](https://doi.org/10.1038/s41567-020-0967-9).
- 889 [48] J. Ahn and B.-J. Yang, *Symmetry representation approach to topological*
890 *invariants in $C_{2z}T$ -symmetric systems*, Phys. Rev. B **99**, 235125 (2019),
891 doi:[10.1103/PhysRevB.99.235125](https://doi.org/10.1103/PhysRevB.99.235125).
- 892 [49] J. Ahn, S. Park and B.-J. Yang, *Failure of Nielsen-Ninomiya theorem and frag-*
893 *ile topology in two-dimensional systems with space-time inversion symmetry: Applica-*
894 *tion to twisted bilayer graphene at magic angle*, Phys. Rev. X **9**, 021013 (2019),
895 doi:[10.1103/PhysRevX.9.021013](https://doi.org/10.1103/PhysRevX.9.021013).
- 896 [50] J. Ahn, S. Park, D. Kim, Y. Kim and B.-J. Yang, *Stiefel–Whitney classes and topologi-*
897 *cal phases in band theory*, Chin. Phys. B **28**(11), 117101 (2019), doi:[10.1088/1674-](https://doi.org/10.1088/1674-1056/ab4d3b)
898 [1056/ab4d3b](https://doi.org/10.1088/1674-1056/ab4d3b).
- 899 [51] H. C. Po, H. Watanabe and A. Vishwanath, *Fragile topology and Wannier obstructions*,
900 Phys. Rev. Lett. **121**, 126402 (2018), doi:[10.1103/PhysRevLett.121.126402](https://doi.org/10.1103/PhysRevLett.121.126402).
- 901 [52] F. N. Ünal, A. Bouhon and R.-J. Slager, *Topological Euler class as a dy-*
902 *namical observable in optical lattices*, Phys. Rev. Lett. **125**, 053601 (2020),
903 doi:[10.1103/PhysRevLett.125.053601](https://doi.org/10.1103/PhysRevLett.125.053601).
- 904 [53] Y. Guan, A. Bouhon and O. V. Yazyev, *Landau levels of the Euler class topology*, Phys. Rev.
905 Res. **4**, 023188 (2022), doi:[10.1103/PhysRevResearch.4.023188](https://doi.org/10.1103/PhysRevResearch.4.023188).
- 906 [54] F. Xie, Z. Song, B. Lian and B. A. Bernevig, *Topology-bounded superfluid*
907 *weight in twisted bilayer graphene*, Phys. Rev. Lett. **124**, 167002 (2020),
908 doi:[10.1103/PhysRevLett.124.167002](https://doi.org/10.1103/PhysRevLett.124.167002).

- 909 [55] A. Bouhon, T. c. v. Bzdušek and R.-J. Slager, *Geometric approach to frag-*
910 *ile topology beyond symmetry indicators*, Phys. Rev. B **102**, 115135 (2020),
911 doi:[10.1103/PhysRevB.102.115135](https://doi.org/10.1103/PhysRevB.102.115135).
- 912 [56] A. Kitaev, *Periodic table for topological insulators and superconductors*, AIP Conf. Proc.
913 **1134**(1), 22 (2009), doi:[10.1063/1.3149495](https://doi.org/10.1063/1.3149495).
- 914 [57] B. Peng, A. Bouhon, B. Monserrat and R.-J. Slager, *Phonons as a platform for non-*
915 *Abelian braiding and its manifestation in layered silicates*, Nat. Commun. **13**(1), 423
916 (2022), doi:[10.1038/s41467-022-28046-9](https://doi.org/10.1038/s41467-022-28046-9).
- 917 [58] B. Jiang, A. Bouhon, Z.-K. Lin, X. Zhou, B. Hou, F. Li, R.-J. Slager and J.-H. Jiang,
918 *Experimental observation of non-Abelian topological acoustic semimetals and their phase*
919 *transitions*, Nature Physics **17**(11), 1239 (2021), doi:[10.1038/s41567-021-01340-x](https://doi.org/10.1038/s41567-021-01340-x).
- 920 [59] H. Qiu, Q. Zhang, T. Liu, X. Fan, F. Zhang and C. Qiu, *Minimal non-abelian nodal braiding*
921 *in ideal metamaterials*, Nat. Commun. **14**(1), 1261 (2023), doi:[10.1038/s41467-023-](https://doi.org/10.1038/s41467-023-36952-9)
922 [36952-9](https://doi.org/10.1038/s41467-023-36952-9).
- 923 [60] M. Wang, S. Liu, Q. Ma, R.-Y. Zhang, D. Wang, Q. Guo, B. Yang, M. Ke, Z. Liu and C. T.
924 Chan, *Experimental observation of non-Abelian earring nodal links in phononic crystals*,
925 Phys. Rev. Lett. **128**, 246601 (2022), doi:[10.1103/PhysRevLett.128.246601](https://doi.org/10.1103/PhysRevLett.128.246601).
- 926 [61] E. Yang, B. Yang, O. You, H.-C. Chan, P. Mao, Q. Guo, S. Ma, L. Xia, D. Fan, Y. Xiang
927 and S. Zhang, *Observation of non-Abelian nodal links in photonics*, Phys. Rev. Lett. **125**,
928 033901 (2020), doi:[10.1103/PhysRevLett.125.033901](https://doi.org/10.1103/PhysRevLett.125.033901).
- 929 [62] Q. Guo, T. Jiang, R.-Y. Zhang, L. Zhang, Z.-Q. Zhang, B. Yang, S. Zhang and C. T. Chan,
930 *Experimental observation of non-Abelian topological charges and edge states*, Nature
931 **594**(7862), 195 (2021), doi:[10.1038/s41586-021-03521-3](https://doi.org/10.1038/s41586-021-03521-3).
- 932 [63] D. Wang, B. Yang, M. Wang, R.-Y. Zhang, X. Li, Z. Q. Zhang, S. Zhang and C. T. Chan,
933 *Observation of non-Abelian charged nodes linking nonadjacent gaps*, Phys. Rev. Lett. **129**,
934 263604 (2022), doi:[10.1103/PhysRevLett.129.263604](https://doi.org/10.1103/PhysRevLett.129.263604).
- 935 [64] D. Wang, Y. Wu, Z. Q. Zhang and C. T. Chan, *Non-Abelian frame charge flow in photonic*
936 *media*, Phys. Rev. X **13**, 021024 (2023), doi:[10.1103/PhysRevX.13.021024](https://doi.org/10.1103/PhysRevX.13.021024).
- 937 [65] W. Zhao, Y.-B. Yang, Y. Jiang, Z. Mao, W. Guo, L. Qiu, G. Wang, L. Yao, L. He, Z. Zhou,
938 Y. Xu and L. Duan, *Quantum simulation for topological Euler insulators*, Commun. Phys.
939 **5**(1), 223 (2022), doi:[10.1038/s42005-022-01001-2](https://doi.org/10.1038/s42005-022-01001-2).
- 940 [66] B. Jiang, A. Bouhon, S.-Q. Wu, Z.-L. Kong, Z.-K. Lin, R.-J. Slager and J.-H. Jiang, *Exper-*
941 *imental observation of meronic topological acoustic Euler insulators* (2022), [2205.03429](https://doi.org/10.1038/s41567-022-03429-2).
- 942 [67] O. Breach, R.-J. Slager and F. N. Ünal, *Interferometry of non-Abelian band singularities*
943 *and Euler class topology* (2024), [2401.01928](https://doi.org/10.1038/s41567-024-01928-2).
- 944 [68] W. J. Jankowski, A. S. Morris, A. Bouhon, F. N. Ünal and R.-J. Slager, *Optical manifes-*
945 *tations of topological Euler class in electronic materials* (2023), [2311.07545](https://doi.org/10.1038/s41567-023-07545-2).
- 946 [69] C. Fang and L. Fu, *New classes of three-dimensional topological crystalline in-*
947 *ulators: Nonsymmorphic and magnetic*, Phys. Rev. B **91**, 161105 (2015),
948 doi:[10.1103/PhysRevB.91.161105](https://doi.org/10.1103/PhysRevB.91.161105).

- 949 [70] C. Wang, F. Liu and H. Huang, *Effective model for fractional topologi-*
950 *cal corner modes in quasicrystals*, Phys. Rev. Lett. **129**, 056403 (2022),
951 doi:[10.1103/PhysRevLett.129.056403](https://doi.org/10.1103/PhysRevLett.129.056403).
- 952 [71] H. Huang, J. Fan, D. Li and F. Liu, *Generic orbital design of higher-order topological*
953 *quasicrystalline insulators with odd five-fold rotation symmetry*, Nano Lett. **21**(16), 7056
954 (2021), doi:[10.1021/acs.nanolett.1c02661](https://doi.org/10.1021/acs.nanolett.1c02661).
- 955 [72] R. Chen, C.-Z. Chen, J.-H. Gao, B. Zhou and D.-H. Xu, *Higher-order topo-*
956 *logical insulators in quasicrystals*, Phys. Rev. Lett. **124**, 036803 (2020),
957 doi:[10.1103/PhysRevLett.124.036803](https://doi.org/10.1103/PhysRevLett.124.036803).
- 958 [73] D. Varjas, A. Lau, K. Pöyhönen, A. R. Akhmerov, D. I. Pikulin and I. C. Fulga, *Topo-*
959 *logical phases without crystalline counterparts*, Phys. Rev. Lett. **123**, 196401 (2019),
960 doi:[10.1103/PhysRevLett.123.196401](https://doi.org/10.1103/PhysRevLett.123.196401).
- 961 [74] S. Spurrier and N. R. Cooper, *Kane-mele with a twist: Quasicrystalline higher-order*
962 *topological insulators with fractional mass kinks*, Phys. Rev. Res. **2**, 033071 (2020),
963 doi:[10.1103/PhysRevResearch.2.033071](https://doi.org/10.1103/PhysRevResearch.2.033071).
- 964 [75] D. V. Else, S.-J. Huang, A. Prem and A. Gromov, *Quantum many-body topology of qua-*
965 *sicrystals*, Phys. Rev. X **11**, 041051 (2021), doi:[10.1103/PhysRevX.11.041051](https://doi.org/10.1103/PhysRevX.11.041051).
- 966 [76] C.-A. Li, B. Fu, Z.-A. Hu, J. Li and S.-Q. Shen, *Topological phase transitions in*
967 *disordered electric quadrupole insulators*, Phys. Rev. Lett. **125**, 166801 (2020),
968 doi:[10.1103/PhysRevLett.125.166801](https://doi.org/10.1103/PhysRevLett.125.166801).
- 969 [77] W. A. Benalcazar and A. Cerjan, *Chiral-symmetric higher-order topological phases of*
970 *matter*, Phys. Rev. Lett. **128**, 127601 (2022), doi:[10.1103/PhysRevLett.128.127601](https://doi.org/10.1103/PhysRevLett.128.127601).
- 971 [78] A. Agarwala, V. Juričić and B. Roy, *Higher-order topological insulators in amorphous*
972 *solids*, Phys. Rev. Res. **2**, 012067 (2020), doi:[10.1103/PhysRevResearch.2.012067](https://doi.org/10.1103/PhysRevResearch.2.012067).
- 973 [79] J.-H. Wang, Y.-B. Yang, N. Dai and Y. Xu, *Structural-disorder-induced second-order*
974 *topological insulators in three dimensions*, Phys. Rev. Lett. **126**, 206404 (2021),
975 doi:[10.1103/PhysRevLett.126.206404](https://doi.org/10.1103/PhysRevLett.126.206404).
- 976 [80] Y.-L. Tao, J.-H. Wang and Y. Xu, *Average symmetry protected higher-*
977 *order topological amorphous insulators*, SciPost Phys. **15**, 193 (2023),
978 doi:[10.21468/SciPostPhys.15.5.193](https://doi.org/10.21468/SciPostPhys.15.5.193).
- 979 [81] Y.-B. Yang, J.-H. Wang, K. Li and Y. Xu, *Higher-order topological phases in crystalline*
980 *and non-crystalline systems: a review*, Journal of Physics: Condensed Matter **36**(28),
981 283002 (2024), doi:[10.1088/1361-648X/ad3abd](https://doi.org/10.1088/1361-648X/ad3abd).
- 982 [82] M. Nakahara, *Geometry, topology and physics*, CRC press (2018).
- 983 [83] J. Bellissard, A. van Elst and H. Schulz-Baldes, *The noncommutative geometry of the*
984 *quantum Hall effect*, J. Math. Phys. (N.Y.) **35**(10), 5373 (1994).
- 985 [84] N. Marzari and D. Vanderbilt, *Maximally localized generalized Wannier functions for com-*
986 *posite energy bands*, Phys. Rev. B **56**, 12847 (1997), doi:[10.1103/PhysRevB.56.12847](https://doi.org/10.1103/PhysRevB.56.12847).
- 987 [85] N. Marzari, A. A. Mostofi, J. R. Yates, I. Souza and D. Vanderbilt, *Maximally local-*
988 *ized Wannier functions: Theory and applications*, Rev. Mod. Phys. **84**, 1419 (2012),
989 doi:[10.1103/RevModPhys.84.1419](https://doi.org/10.1103/RevModPhys.84.1419).

- 990 [86] A. A. Soluyanov and D. Vanderbilt, *Wannier representation of Z_2 topological insulators*,
991 Phys. Rev. B **83**, 035108 (2011), doi:[10.1103/PhysRevB.83.035108](https://doi.org/10.1103/PhysRevB.83.035108).
- 992 [87] C. Brouder, G. Panati, M. Calandra, C. Mourougane and N. Marzari, *Exponential lo-*
993 *calization of Wannier functions in insulators*, Phys. Rev. Lett. **98**, 046402 (2007),
994 doi:[10.1103/PhysRevLett.98.046402](https://doi.org/10.1103/PhysRevLett.98.046402).
- 995 [88] E. Prodan, *On the generalized Wannier functions*, J. Math. Phys. **56**(11), 113511 (2015),
996 doi:[10.1063/1.4936303](https://doi.org/10.1063/1.4936303).
- 997 [89] H. D. Cornean, I. Herbst and G. Nenciu, *On the construction of composite Wannier*
998 *functions*, Annales Henri Poincaré **17**(12), 3361 (2016), doi:[10.1007/s00023-016-](https://doi.org/10.1007/s00023-016-0489-2)
999 [0489-2](https://doi.org/10.1007/s00023-016-0489-2).
- 1000 [90] D. Fiorenza, D. Monaco and G. Panati, *Construction of real-valued localized com-*
1001 *posite wannier functions for insulators*, Annales Henri Poincaré **17**(1), 63 (2016),
1002 doi:[10.1007/s00023-015-0400-6](https://doi.org/10.1007/s00023-015-0400-6).
- 1003 [91] T. M. Gunawardana, A. M. Turner and R. Barnett, *Optimally localized single-band Wan-*
1004 *nier functions for two-dimensional Chern insulators*, Phys. Rev. Res. **6**, 023046 (2024),
1005 doi:[10.1103/PhysRevResearch.6.023046](https://doi.org/10.1103/PhysRevResearch.6.023046).
- 1006 [92] D. Monaco, G. Panati, A. Pisante and S. Teufel, *Optimal decay of Wannier functions in*
1007 *Chern and quantum Hall insulators*, Communications in Mathematical Physics **359**(1),
1008 61 (2018), doi:[10.1007/s00220-017-3067-7](https://doi.org/10.1007/s00220-017-3067-7).
- 1009 [93] J. Zhu, Z. Chen and B. Wu, *Construction of Wannier functions in disordered systems*
1010 (2015), [1512.02043](https://arxiv.org/abs/1512.02043).
- 1011 [94] J. C. Slater and G. F. Koster, *Simplified LCAO method for the periodic potential problem*,
1012 Phys. Rev. **94**, 1498 (1954), doi:[10.1103/PhysRev.94.1498](https://doi.org/10.1103/PhysRev.94.1498).
- 1013 [95] D. Li, M. Pan, C. Wang and H. Huang, *Angular momentum invoked band inversions*
1014 *in mirror symmetry protected topological states*, Phys. Rev. B **105**, 195133 (2022),
1015 doi:[10.1103/PhysRevB.105.195133](https://doi.org/10.1103/PhysRevB.105.195133).
- 1016 [96] W. A. Harrison, *Electronic structure and the properties of solids: the physics of the chemical*
1017 *bond*, Courier Corporation (2012).
- 1018 [97] T. Takagi, *On an algebraic problem related to an analytic theorem of Carathéodory and Fe-*
1019 *jér and on an allied theorem of Landau*, In *Japanese journal of mathematics: transactions*
1020 *and abstracts*, vol. 1, pp. 83–93. The Mathematical Society of Japan (1924).
- 1021 [98] P. M. Lenggenhager, X. Liu, T. Neupert and B. Tomas, *Universal higher-order bulk-*
1022 *boundary correspondence of triple nodal points*, Phys. Rev. B **106**, 085129 (2022),
1023 doi:[10.1103/PhysRevB.106.085129](https://doi.org/10.1103/PhysRevB.106.085129).
- 1024 [99] W. J. Jankowski, M. Noormandipour, A. Bouhon and R.-J. Slager, *Disorder-induced topo-*
1025 *logical quantum phase transitions in Euler semimetals* (2023), [2306.13084](https://arxiv.org/abs/2306.13084).
- 1026 [100] F.-J. Wang, Z.-Y. Xiao, R. Queiroz, B. A. Bernevig, A. Stern and Z.-D. Song, *Anderson*
1027 *critical metal phase in trivial states protected by average magnetic crystalline symmetry*,
1028 Nature Communications **15**(1), 3069 (2024), doi:[10.1038/s41467-024-47467-2](https://doi.org/10.1038/s41467-024-47467-2).
- 1029 [101] H. Huang and F. Liu, *A unified view of topological phase transition in band theory*, Re-
1030 search **2020**, 7832610 (2020), doi:[10.34133/2020/7832610](https://doi.org/10.34133/2020/7832610).

- 1031 [102] X. Ni, H. Huang and F. Liu, *Robustness of topological insulating phase against vacancy,*
1032 *vacancy cluster, and grain boundary bulk defects*, Phys. Rev. B **101**, 125114 (2020),
1033 doi:[10.1103/PhysRevB.101.125114](https://doi.org/10.1103/PhysRevB.101.125114).
- 1034 [103] C. Wang, T. Cheng, Z. Liu, F. Liu and H. Huang, *Structural amorphization-*
1035 *induced topological order*, Phys. Rev. Lett. **128**, 056401 (2022),
1036 doi:[10.1103/PhysRevLett.128.056401](https://doi.org/10.1103/PhysRevLett.128.056401).
- 1037 [104] K. D. Stubbs, A. B. Watson and J. Lu, *Iterated projected position algorithm for con-*
1038 *structing exponentially localized generalized wannier functions for periodic and nonpe-*
1039 *riodic insulators in two dimensions and higher*, Phys. Rev. B **103**, 075125 (2021),
1040 doi:[10.1103/PhysRevB.103.075125](https://doi.org/10.1103/PhysRevB.103.075125).
- 1041 [105] J. Langbehn, Y. Peng, L. Trifunovic, F. von Oppen and P. W. Brouwer, *Reflection-symmetric*
1042 *second-order topological insulators and superconductors*, Phys. Rev. Lett. **119**, 246401
1043 (2017), doi:[10.1103/PhysRevLett.119.246401](https://doi.org/10.1103/PhysRevLett.119.246401).
- 1044 [106] A. Bouhon and R.-J. Slager, *Multi-gap topological conversion of Euler class via band-node*
1045 *braiding: minimal models, PT-linked nodal rings, and chiral heirs* (2022), [2203.16741](https://arxiv.org/abs/2203.16741).
- 1046 [107] M. J. Park, Y. Kim, G. Y. Cho and S. Lee, *Higher-order topological in-*
1047 *insulator in twisted bilayer graphene*, Phys. Rev. Lett. **123**, 216803 (2019),
1048 doi:[10.1103/PhysRevLett.123.216803](https://doi.org/10.1103/PhysRevLett.123.216803).
- 1049 [108] E. Lee, R. Kim, J. Ahn and B.-J. Yang, *Two-dimensional higher-order topology in mono-*
1050 *layer graphdiyne*, npj Quantum Materials **5**(1), 1 (2020), doi:[10.1038/s41535-019-](https://doi.org/10.1038/s41535-019-0206-8)
1051 [0206-8](https://doi.org/10.1038/s41535-019-0206-8).
- 1052 [109] X.-L. Sheng, C. Chen, H. Liu, Z. Chen, Z.-M. Yu, Y. X. Zhao and S. A. Yang, *Two-*
1053 *dimensional second-order topological insulator in graphdiyne*, Phys. Rev. Lett. **123**,
1054 256402 (2019), doi:[10.1103/PhysRevLett.123.256402](https://doi.org/10.1103/PhysRevLett.123.256402).
- 1055 [110] M. Pan and H. Huang, *Phononic stiefel-whitney topology with corner vibrational modes in*
1056 *two-dimensional xenes and ligand-functionalized derivatives*, Phys. Rev. B **106**, L201406
1057 (2022), doi:[10.1103/PhysRevB.106.L201406](https://doi.org/10.1103/PhysRevB.106.L201406).
- 1058 [111] M. Pan, D. Li, J. Fan and H. Huang, *Two-dimensional Stiefel-Whitney insulators in lig-*
1059 *anded Xenes*, npj Comput. Mater. **8**, 1 (2022), doi:[10.1038/s41524-021-00695-2](https://doi.org/10.1038/s41524-021-00695-2).